Chemical Engineering Journal 491 (2024) 151668

Contents lists available at ScienceDirect

Chemical Engineering Journal

journal homepage: www.elsevier.com/locate/cej

# The role of reverse Boudouard reaction during integrated $CO_2$ capture and utilisation via dry reforming of methane

Xiaotong Zhao [a,1], Shuzhuang Sun [a,1], Yuanyuan Wang [a], Yingrui Zhang [a], Yuan Zhu [a], Bo Zong [a], Jia Hu [a], Paul Williams [b,*], Chunfei Wu [a,*]

[a] School of Chemistry and Chemical Engineering, Queen's University Belfast, Belfast BT7 1NN, UK
[b] School of Chemical and Process Engineering University of Leeds, Leeds LS2 9JT, UK

ARTICLE INFO

*Keywords:*
Integrated $CO_2$ capture and utilisation (ICCU)
Dry reforming of methane (DRM)
Dual-functional materials (DFMs)
Synergistic effects

ABSTRACT

Integrated carbon capture and utilisation (ICCU) is an emerging technology for simultaneous $CO_2$ adsorption and conversion into value-added products. This provides a more sustainable approach compared to carbon capture and storage. Dual-functional materials (DFMs) that couple $CO_2$ sorbents (e.g. CaO) and catalysts (e.g. Ni) enable direct utilisation of sorbed $CO_2$ for reactions like dry reforming of methane (DRM). However, the potential interactions between sorbent and catalyst components within DFMs may induce distinct mechanisms compared to individual materials. Elucidating these synergies and interfacial phenomena is vital for guiding the rational design of DFMs. This article investigates the respective roles of $Ni/SiO_2$ catalyst and sol–gel synthesised CaO sorbent in integrated $CO_2$ capture and utilisation via dry reforming of methane (ICCU-DRM) using a decoupling approach. Through decoupled reactor experiments, it is found that $Ni/SiO_2$ activates $CO_2$ to react with carbon deposits from $CH_4$ decomposition, achieving maximal CO and $H_2$ yields of 43.41 mmol $g^{-1}$ and 46.78 mmol $g^{-1}$ as well as 87.2 % $CO_2$ conversion at 650 °C. Characterisation shows that coke would encapsulate Ni nanoparticles and be active for $CO_2$ conversion via Boudouard reaction, indicating sufficient catalyst-sorbent contact is necessary for $CO_2$ spillover. In-situ DRIFTS reveals that no obvious $CH_4$-$CaCO_3$ reaction occurs, $CO_2$ chemisorption on $Ni/SiO_2$ enables the reverse Boudouard reaction, which is further verified by DFT calculations. The findings elucidate the dependent and synergistic roles of $Ni/SiO_2$ and $CaO/CaCO_3$ in ICCU-DRM, and highlight the importance of catalyst-adsorbent interactions in optimising dual-functional materials.

## 1. Introduction

The escalation of the greenhouse effect due to significant $CO_2$ emissions from industrial activities necessitates $CO_2$ reduction strategies [1]. Integrated Carbon Capture and Utilization (ICCU), a novel technology combining $CO_2$ adsorption and conversion, has gained prominence for its potential in $CO_2$ emission mitigation [2,3]. This approach, superior to carbon capture and storage (CCS), eliminates storage costs and minimises leakage risks [4]. Utilising dual-function materials (DFMs) that amalgamate catalysts and $CO_2$ sorbents, ICCU achieves concurrent $CO_2$ capture and conversion [5,6]. This approach enhances $CO_2$ conversion by directly reacting reductive gases with $CO_2$-loaded sorbents, outperforming the conventional $CO_2$ catalytic processes [7]. For a typical ICCU process, $CO_2$-containing exhaust gases (e.g. flue gas) are first absorbed by DFMs [8], then reacted with reducing agents like $H_2$ or $CH_4$, simultaneously generating useful products and regenerating the sorbent [2]. Current research trends focus on ICCU-RWGS (reverse water–gas shift) using $H_2$ as a reducing agent, noted for its mild reaction conditions and suitability for industrial applications [9]. However, $H_2$ sourcing remains a critical challenge [10], especially considering that over 50 % of global $H_2$ is produced by $CO_2$-intensive steam methane reforming (SMR) processes [11]. This paradoxically undermines the $CO_2$ reduction goal of ICCU. As a result, the attention is shifting towards ICCU via dry reforming of methane (ICCU-DRM), which utilises $CH_4$, another greenhouse gas, offering a dual mitigation approach for $CO_2$ and $CH_4$ emissions. This approach, leveraging the wider availability of $CH_4$ from sources like fossil fuels [12], agriculture [13], and waste management [14], presents a more sustainable and economical alternative. Moreover, ICCU-DRM produces both CO and $H_2$, which could be further upgraded into valuable chemicals [15].

* Corresponding authors.
*E-mail addresses:* p.t.williams@leeds.ac.uk (P. Williams), c.wu@qub.ac.uk (C. Wu).
[1] Co-first Author.

https://doi.org/10.1016/j.cej.2024.151668

Available online 26 April 2024

Achieving simultaneous adsorption and conversion of $CO_2$ using DFMs is the key to ICCU. In the context of $CO_2$ adsorption, calcium oxide (CaO) is known for its high capacity and kinetics in reacting with $CO_2$, as depicted in Reaction (1) [16]. Its widespread use is attributed to both its low cost and substantial $CO_2$ capacity [17]. Notably, recent studies have demonstrated that unprocessed natural marble, primarily consisting of CaO [18], also possesses effective $CO_2$ adsorption capabilities. This discovery has substantial implications for reducing the production costs of $CO_2$ adsorbents, further reinforcing the advantages of CaO in such applications. However, a significant issue with CaO-based sorbents in ICCU is their tendency to sinter over multiple cycles, which results in a decreased $CO_2$ capacity. Consequently, numerous studies are dedicated to enhancing the cyclic stability of CaO. For instance, Sun et al. integrated $CeO_2$ into CaO, achieving excellent stability over 20 cycles of reactions [19]. Additionally, Wu and colleagues have synthesised CaO-based sorbents using the sol–gel method, achieving $CO_2$ conversion rates exceeding 90 %[20].

In the context of $CO_2$ conversion during ICCU-DRM, the extensively studied mechanism of conventional DRM provided critical insights for catalyst development based on transition-metal-based catalysts, including Nickel (Ni) [21], Ruthenium (Ru), Cobalt (Co)[22], etc. A typical DRM process encompasses a four-step dehydrogenation of $CH_4$ (Reaction (2)–Reaction (5) and subsequent reactions with $CO_2$, believed to be an oxidant, and the dehydrogenation products of $CH_4$ [23]. However, a simulation study on Ni-based catalysts suggested that the primary oxidant in the DRM process originated from the dehydrogenation of hydroxyl groups [24]. Despite different perspectives, the importance of $CH_4$ decomposition is widely recognised in the DRM process. This is underscored by a mechanistic analysis, which, upon calculating the activation energies of each DRM stage, highlights $CH_4$ dehydrogenation as the critical, rate-limiting step [25]. Typically, $CH_4$ dehydrogenation in DRM results in solid carbon deposits that can hinder catalyst performance by covering active sites [26]. Consequently, extensive research is being conducted to address carbon deposition, yielding promising results [27]. For instance, Yang et al. developed Core@shell Ni@Co nanoparticles with controlled Co/Ni compositions and discovered that an increased Co content in Ni@$Co_x$/$CeO_2$ enhances coke resistance [28].

$$CaO + CO_2 = CaCO_3 \quad \text{Reaction (1)}$$

$$CH_4 = CH_3^* + H^* \quad \text{Reaction (2)}$$

$$CH_3^* = CH_2^* + H^* \quad \text{Reaction (3)}$$

$$CH_2^* = CH^* + H^* \quad \text{Reaction (4)}$$

$$CH^* = C^* + H^* \quad \text{Reaction (5)}$$

Although the individual functions of adsorbents and catalysts in $CO_2$ adsorption and DRM have been extensively researched, it is important to recognise the potential interactions between these components in DFMs that can lead to distinct mechanisms in ICCU-DRM [17]. For example, a recent study, utilising calcium-fortified hydroxyapatite (HAP) as the adsorbent and Ni as the catalyst, demonstrated that the augmentation of HAP via Ca incorporation notably enhanced the catalytic efficiency, thereby elevating the $CO_2$ conversion rate in the ICCU process [29]. Another research indicated that enhancing the distribution of Ni catalysts on CaO adsorbent surfaces increased CO yield in ICCU-DRM processes [30]. Our previous study also reported that the Ni catalysts would be encapsulated by CaO adsorbents during carbonation in oxygen-rich and humid environments, thereby diminishing the performance of DFMs [31]. The outcomes of these studies indirectly confirm the differences in the reaction mechanisms of ICCU-DRM and traditional DRM due to the interaction between catalysts and adsorbents, which are critical for the design of effective DFMs. Notably, one study revealed a process in ICCU-RWGS where $H_2$ directly reacted with $CaCO_3$ to produce CO, bypassing the need for a catalyst [7,32]. Furthermore, Wang et al. conducted a simulation study that revealed the surface of $CaCO_3$ can adsorb $H_2$, thereby facilitating the formation of bicarbonate ions, enabling the direct utilisation of $CaCO_3$ and $H_2$ to produce CO [33]. The new finding introduces novel potential reaction pathways for the ICCU-DRM process. It encompasses a detailed investigation into the potential chemical interaction between $H_2$, produced from the decomposition of $CH_4$, and $CaCO_3$. Additionally, it explores whether the coke, a byproduct formed during the $CH_4$ decomposition, exhibits reactivity with $CaCO_3$. Current research has yet to provide answers to these newly emerged possibilities. Therefore, it is necessary to conduct research that reveals both the distinct roles of adsorbents and catalysts and the potential interplay between them in ICCU-DRM for the advancement of more effective DFMs.

Herein, we adopted a decoupling research approach for DFMs. Specifically, we prepared sol–gel CaO and Ni/$SiO_2$ as separate adsorbents and catalysts. The materials were arranged in the reaction tube in different configurations: uniformly physically mixed, CaO followed by Ni/$SiO_2$, Ni/$SiO_2$ followed by CaO, and individual CaO and Ni/$SiO_2$. ICCU-DRM experiments were carried out with the same condition for these five scenarios to compare $CO_2$ uptake, CO yield, $H_2$ yield, and $CO_2$ conversion as performance metrics, analysing the respective roles of the adsorbent and catalyst throughout the process. More importantly, through the decoupling approach, we aim to ascertain whether the interaction between the adsorbent and catalyst within DFMs inherently impacts DFM performance. This notion has been suggested in previous research, yet there currently lacks direct experimental evidence to substantiate it. Additionally, material characterisation using SEM, TEM, TGA, XRD, Raman, in situ DRIFTS, and DFT simulations have been conducted to compare the reactions that the adsorbents and catalysts individually facilitate with $CO_2$ and $CH_4$, thereby analysing potential interactions that may influence the ICCU-DRM process.

## 2. Experimental section

### 2.1. Materials synthesis

The synthesis of CaO was conducted utilising the sol–gel combustion method, as delineated in prior reports [34]. The process involved dissolving $Ca(NO_3)_2{\cdot}6H_2O$ (Sigma-Aldrich, > 99.0 %) and citric acid (Sigma-Aldrich, > 99.5 %) in distilled water. This mixture was continuously stirred for one hour at ambient temperature, adhering to a molar ratio of $Ca^{2+}$: $C_6H_8O_7$: $H_2O$ = 10:100: 4000. Subsequently, the solution underwent evaporation at 90 °C with stirring, leading to the formation of a viscous gel followed by drying at 130 °C overnight. The resultant product was finely ground and calcined in a Muffle furnace in still air. The calcination was executed at a ramp rate of 5 °C per minute up to 800 °C and maintained for 5 h, culminating in the production of sol–gel CaO powder.

A Ni/$SiO_2$ catalyst, employed for DRM, was synthesised via the wet impregnation method. $Ni(NO_3)_2{\cdot}6H_2O$ (Sigma-Aldrich, > 99.0 %) and $SiO_2$ (Sigma-Aldrich, > 99.0 %) were solubilised in distilled water under continuous stirring at ambient conditions for one hour. The mass ratio maintained was $Ni(NO_3)_2{\cdot}6H_2O$: $SiO_2$: $H_2O$ = 1.09: 2.0: 20. This mixture was then subjected to evaporation at 95 °C with stirring, followed by a drying stage in an oven at 130 °C for 12 h. Subsequently, the resultant material was pulverised into a fine powder and subjected to calcination in a static air environment within the Muffle furnace. The calcination process involved a heating rate of 5 °C per minute up to 800 °C, maintained for 3 h, to synthesise the preliminary NiO/$SiO_2$ catalyst. The final step involved the reduction of this catalyst at 700 °C for one hour in a 5.0 % $H_2$/Ar atmosphere at a flow rate of 100 mL $min^{-1}$, yielding the reduced Ni/$SiO_2$ catalyst. To analyse the coke formed on the Ni/$SiO_2$, the coked Ni/$SiO_2$ sample was prepared under 10 % $CH_4$/$N_2$ with the flow rate of 100 mL $min^{-1}$ by the reduced Ni/$SiO_2$ catalyst at 650 °C for

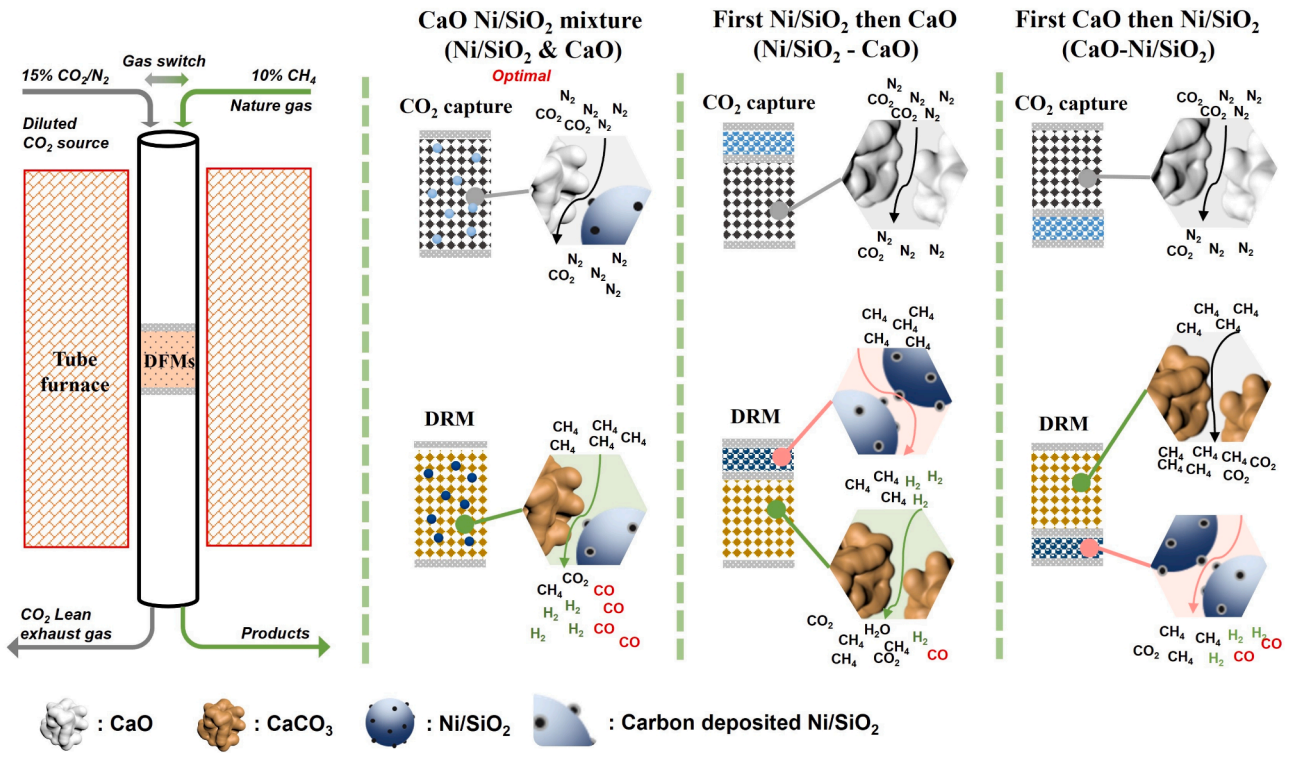


**Fig.1.** Schematic diagram of ICCU-DRM evaluation system.

2 h.

### 2.2. Material characterisations and computational methods

The phase compositions of $Ni/SiO_2$ subjected to $CH_4$ treatment and the physically mixed CaO-$Ni/SiO_2$ after ICCU-DRM and the subsequent $CO_2$ treatments were elucidated using powder X-ray diffraction (XRD). The $CO_2$ treatment can remove the coke on $Ni/SiO_2$ via reverse Boudouard reaction. This analysis was performed on a PANalytical Empyrean series 2 diffractometer, equipped with a Cu Kα X-ray source, operating over a 2θ range of 5–80°. The Raman spectra were collected on the WITec Alpha 300R Confocal Raman Microscope, which was equipped with a 532 nm diode laser (10 mW). Temperature-programmed reduction (TPR) and oxidation (TPO) profiles were obtained using a Hi-Res TGA 2950 thermogravimetric analyser. In the $H_2$-TPR process, $NiO/SiO_2$ was initially pretreated at 800 °C for 10 min, followed by stabilisation at 200 °C in $N_2$. Thereafter, a 5.0 % $H_2$/Ar mixture was introduced, with a temperature increase of 10 °C per min up to 800 °C. The TPO tests were conducted after $H_2$-TPR, involving the same temperature condition in 21 % $O_2/N_2$ mixture. 10 % $CH_4/N_2$ and 15 % $CO_2/N_2$ were respectively applied for $CH_4$-TPR and $CO_2$-TPO, following the similar temperature program. A FEI Helios G4 CX Dual Beam high resolution monochromate field emission gun (FEG) scanning electron microscope (SEM) and transmission electron microscopy (TEM, JEOL 2010) were used to characterise the morphology of the coked $Ni/SiO_2$, ICCU-DRM treated or $CO_2$ recovered CaO-$Ni/SiO_2$ to analyse the coke formed on the $Ni/SiO_2$ surface. In-situ diffuse reflectance infrared Fourier transform spectroscopy (DRIFTS) with a high-temperature cell (PIKE technology, UK) was used to analyse the sorption process under $CO_2$ and the catalytic process under $CH_4$ for the sol–gel CaO and $Ni/SiO_2$. Specifically, the materials were adsorbed by 15 % $CO_2/N_2$ for 10 min and then purged with $N_2$ for 3 min, followed by the introduction of a 10 % $CH_4/N_2$ mixture for 30 min. The in situ DRIFTS was also used to analyse the reaction between the coked $Ni/SiO_2$ generated by $CH_4$ pyrolysis and $CaCO_3$ under $N_2$ conditions at 650 °C.

In order to study the catalytic and adsorption properties of Ni and CaO for enhancing the understanding of the interactions between adsorbents and catalysts in the ICCU-DRM process within DFMs, we conducted a computational simulation study which involves: Modeling and optimising Ni (111) and CaO (001) surfaces; Investigating $CO_2$ adsorption on these surfaces; Studying the catalysis of the reverse Boudouard Reaction reaction on them. The study was conducted using spin-polarised electronic structure calculations via the plane-wave basis set in VASP [35], with the PAW method for ion–core electron interactions [36], and a 450 eV cutoff for valence electrons. The PBE functional [37] and DFT-D3 method [38] were employed for electronic exchange, correlation, and van der Waals interactions, respectively. A 15 Å vacuum space and a $3 \times 3 \times 1$ Monkhorst–Pack k-point grid [39] were used, targeting convergence criteria of $10^{-5}$ eV for electronic structure and 0.05 eV/Å for geometry.

### 2.3. ICCU-DRM decouple evaluation

A total of 0.1 g of $Ni/SiO_2$ and 0.2 g of sol–gel CaO were employed in various configurations to evaluate ICCU-DRM performances, aiming to investigate the respective roles of the catalyst and sorbent within DFMs. The selection of $Ni/SiO_2$ catalyst (0.1 g) and CaO adsorbent (0.2 g) was optimized based on previous studies and literature [17], balancing catalytic activity and adsorption capacity against risks like coking and sintering for the former, and dilution of $CO_2$ capacity for the latter. Gas concentration for $CO_2$ was set at 15 % $CO_2/N_2$ to replicate industrial flue gas scenarios [40]. The decision to utilize a 10 % $CH_4/N_2$ concentration was primarily influenced by the need to mitigate coke under high $CH_4$ conditions. Additionally, this concentration aligns with an upper limit of our analytical equipment for $H_2$ concentration analysis, which is 20 %. At 10 % $CH_4/N_2$, even with a $CH_4$ conversion of 100 %, the resulting $H_2$ concentration remains within this analytical threshold, ensuring accurate measurements. As shown in Fig. 1, these configurations included a physically uniform mixture of $Ni/SiO_2$ and sol–gel CaO ($Ni/SiO_2$ & CaO), sequential addition with $Ni/SiO_2$ followed by sol–gel CaO ($Ni/SiO_2$-CaO), an alternative sequence with sol–gel CaO preceding $Ni/SiO_2$ (CaO-$Ni/SiO_2$), as well as isolated applications of $Ni/SiO_2$ and sol–gel

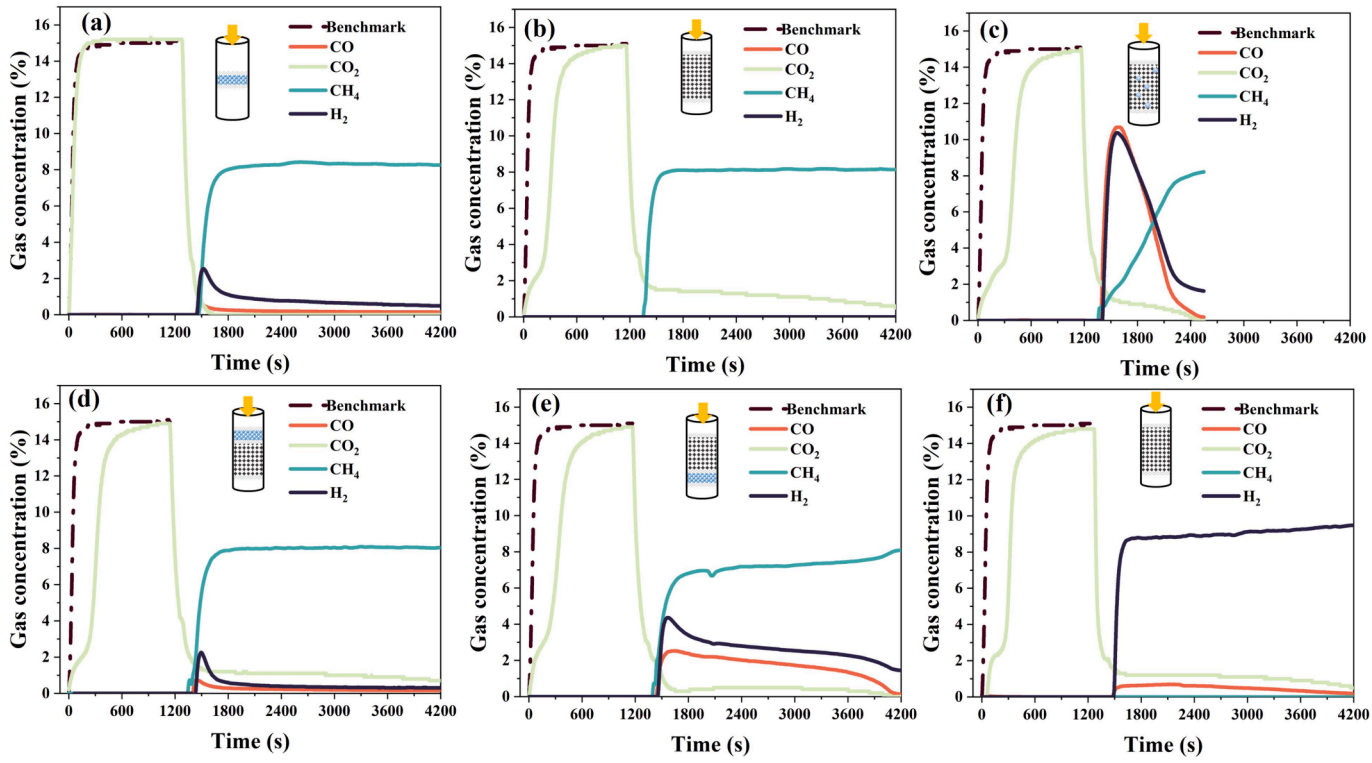


**Fig.2.** ICCU-DRM decouple tests under 15 % $CO_2/N_2$ for 20 min, purged by $N_2$ for 3 min then under 10 % $CH_4/N_2$ until the end of the reaction for different conditions of 0.1 g $Ni/SiO_2$ and 0.2 g sol–gel CaO: (a) is 0.1 g $Ni/SiO_2$ only; (b) is 0.2 g sol–gel CaO only; (c) is $Ni/SiO_2$ & CaO; (d) is $Ni/SiO_2$-CaO; (e) is Cao-$Ni/SiO_2$; (f) is a ICCU-RWGS test for 0.2 g sol gel CaO only under 10 % $H_2/N_2$. All tests were performed at a temperature of 650 °C and a constant gas flow rate of 100 mL $min^{-1}$ in the fixed-bed reactor setup.

CaO. The experimental setup is also shown in Fig. 1. To understand the reactions of $CO_2$ and coke on $Ni/SiO_2$ catalyst and $CaO/CaCO_3$, we conducted experiments at 650 °C under a pure $N_2$ atmosphere at a flow rate of 100 mL $min^{-1}$. In these experiments, $CaCO_3$ (1.0 g) and coked $Ni/SiO_2$ (0.5 g) were sequentially ordered and physically mixed to compare the concentration curves of CO under both scenarios. Similarly, under the same temperature and atmospheric conditions, 1.0 g $CaCO_3$ was mixed with 0.5 g graphene (Sigma-Aldrich, > 99 %) to evaluate the performance of the reverse Boudouard reaction.

The evaluations were conducted in a quartz reaction tube (OD: 12.0 mm; ID: 10.5 mm; L: 650 mm). The quartz tube was fixed in the middle of a tube furnace (Elite TSH 12/50/300-2416CG) for heating. The sample was fixed by quartz wool and placed in the centre of the quartz tube. A thermocouple was placed in the same position as the sample to monitor the temperature. The inlet gases ($CH_4$, $CO_2$, $N_2$, air) were controlled by mass flowmeters (OMEGA FMA-A2306), which were calibrated by a bubble flowmeter. The outlet gases were analysed by a flue gas analyser system, which included a flue gas analyser (Enerac 700 AV; NDIR detector) and an $H_2$ analyser (CX-02; TCD detector). The flow rates of inlet gas were all kept at 100 mL $min^{-1}$. In our study, we have maintained constant inlet and outlet gas flow rates at 100 mL $min^{-1}$, consistent with the methodology employed in the previous research [41,42]. This approach works well when using a feed gas with a lot of $N_2$, which helps keep the effects of chemical reactions on gas volume minimal. Also, considering the small size of our samples with a maximum of 0.5 g, the amount of gas they adsorb is small compared to our steady flow rate. Thus, it is assumed that the outlet flow was constant to simplify the calculations of product yield. In the $CO_2$ capture stage, a 15 % $CO_2/N_2$ mixture was introduced for a duration of 20 min, followed by a 3-minute purge using $N_2$ to clear the reaction tube. Subsequently, during the DRM stage, a 10.0 % $CH_4/N_2$ mixture was fed into the system until the CO concentration, as indicated by the analyser, fell below 0.1 %. The performance of the ICCU-DRM process was assessed through real-time monitoring of $CH_4$, $H_2$, CO, and $CO_2$ concentrations.

The $CO_2$ conversion, CO yield, $H_2$ yield and $CO_2$ uptake were calculated by integrating the real-time data during hydrogenation, as shown in Eq. (1)–Eq. (4) where M (mmol·$s^{-1}g^{-1}$; M = $CO_2$, CO or $CH_4$) represents the real-time flow rate of various fractions. $U_{CO_2}$ (mmol $g^{-1}$), $X_{CO_2}$ (%), $Y_{CO}$ (mmol $g^{-1}$) and $Y_{H_2}$ (mmol $g^{-1}$) represent the $CO_2$ uptake, $CO_2$ conversion, CO yield, and $H_2$ yield.

$$M\ \left(mmol{\cdot}g_{solid}^{-1}{\cdot}s^{-1}\right) = \frac{100\ (mL{\cdot}min^{-1}) \times gas\ con.\ (vol\ \%\ )/100}{60\ (s\ {\cdot}min^{-1}) \times 22.4\ (mL{\cdot}mmol^{\ -1})} \times \frac{1}{mass\ (g_{solid})} \tag{1}$$

$$U_{CO_2}\ \left(mmol{\cdot}g_{solid}^{-1}\right) = \int_0^{20\ min} \left(M_{CO_2}^{benchmark} - M_{CO_2}^{measured}\right) dt \tag{2}$$

$$Y_{CO}\ \left(mmol{\cdot}g_{solid}^{-1}\right) = \int M_{CO}\ dt \tag{3}$$

$$Y_{H_2}\ \left(mmol{\cdot}g_{solid}^{-1}\right) = \int M_{H_2}\ dt \tag{4}$$

$$X_{CO_2}\ (\%\ ) = \frac{\int M_{CO}\ dt}{\int \left(M_{CO}\ + M_{CO_2}^{DRM\ \ stage}\right) dt} \times 100 \tag{5}$$

It should be noted that the integration period for Eq. (2) was set as the experimentally determined duration of the $CO_2$ capture stage, specifically 20 min. Conversely, the integration times for Eq. (5) to Eq. (4) depend on the actual duration of the reaction, that is, from the onset of the DRM stage until the observed decrease of the CO concentration signal to 0.10 % as we reported in the previous research [31].

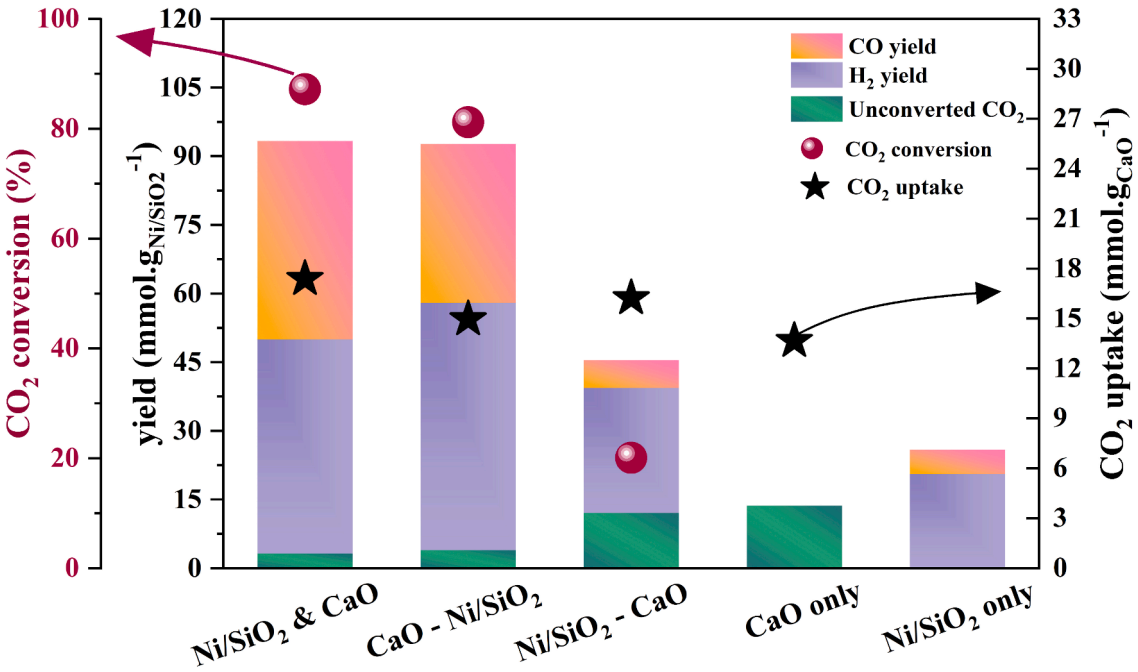


**Fig.3.** Products yield and distribution, $CO_2$ uptake and $CO_2$ conversion in ICCU-DRM decouple tests for $Ni/SiO_2$ & Cao, $Ni/SiO_2$-CaO, CaO-$Ni/SiO_2$, 0.1 g $Ni/SiO_2$ only and 0.2 g sol–gel CaO only.

## 3. Results and discussions

### 3.1. Decoupling performance of ICCU-DRM

Fig. 2 presents the results of the decoupling tests to understand the roles of the catalyst ($Ni/SiO_2$) and adsorbent (sol–gel CaO) in the ICCU-DRM process. A key initial step in ICCU-DRM is $CO_2$ adsorption. During the first 1200 s of all tests depicted in Fig. 2, when the adsorbent is operational, the $CO_2$ concentration at the reactor outlet rises more gradually to 15 % under a 15 % $CO_2/N_2$ atmosphere compared to the benchmark. This observation shows the progressive adsorption of $CO_2$ from the inlet gas by CaO, leading to the gradual saturation of the adsorbent (Reaction (1) [31]. As shown in Fig. 2 (a), in the presence of the catalyst only, the $CO_2$ sorption curve closely aligns with the benchmark curve within the initial 1200 s. It means that the $Ni/SiO_2$ catalyst exhibits negligible $CO_2$ capture capacity. As the surface of $Ni/SiO_2$ is primarily metallic and relatively lacks the basic sites that are typically required for $CO_2$ to chemically adsorb and form stable intermediates [43]. In Fig. 2 (b), where solely the sorbent was present, no signals of CO and $H_2$ were detected during the DRM stage. This indicates that CaO, functioning as a sorbent, inherently lacks the catalytic active sites to facilitate the DRM reaction. The reason should be that CaO does not provide the metal centers required for the activation and dissociation of $CH_4$, a key step in the DRM process [44]. Fig. 2 (c)–(e) demonstrates the results for conditions where both sorbent and catalyst coexist. It is observed that the fastest DRM reaction rate is achieved by $Ni/SiO_2$ & CaO (physical mixture of the two materials), where the reaction completes in nearly 1300 s, as shown in Fig. 2 (c). Concurrently, the peak concentrations of CO and $H_2$ in this setup are the highest among all tests, approximately 10.5 % of each. In contrast, as illustrated in Fig. 2 (d) for $Ni/SiO_2$-CaO ($Ni/SiO_2$ followed by CaO), both CO and $H_2$ concentrations are significantly reduced, with the maximum $H_2$ concentration merely at 2.1 % and CO concentration below 1.0 %. The CO and $H_2$ concentration curves during the DRM stage in Fig. 2 (d) resemble those in Fig. 2 (a), where only the catalyst is present. This suggests that the generated intermediates adhere to the catalyst, thereby limiting their transportation by the gas flow for subsequent interaction with the adsorbed $CO_2$. According to the mechanism of the DRM reaction, the initial step required is the dehydrogenation of $CH_4$ [45]. As high bond energy of $CH_4$ makes its direct interaction with $CO_2$ challenging without this initial dissociation, which is why catalysts are often employed to lower the activation energy required for this step, making the process energetically feasible at lower temperatures [27]. The main products of the $CH_4$ dehydrogenation reaction are $H_2$ and coke [46], and hence the interaction of coke [47] (Reaction 7 and Reaction 8) or $H_2$ (Reaction 9) with $CaCO_3$ [7] is a crucial factor in the formation of CO. If the RWGS reaction between $H_2$ and $CaCO_3$ (Reaction 9) were the primary pathway for CO generation, the observed scenario in Fig. 2 (d) would indicate an alternate behavior, as gaseous $H_2$ is expected to be effectively mobile with the gas flow rather than stationary on the $Ni/SiO_2$ surface. This mobility would typically lead to more significant interactions with $CaCO_3$, resulting in a higher CO concentration, contrasting with the low CO levels seen in Fig. 2 (d). The issue may lie in the fact that the concentration of $H_2$ produced from $CH_4$ cracking is insufficient. At these low $H_2$ levels, there are not enough hydrogen molecules to effectively interact with and reduce $CaCO_3$ [48]. Moreover, the principles of reaction thermodynamics suggest that a more substantial presence of $H_2$ is crucial to drive the reduction process favorably towards CO production (Reaction 9).

Another piece of evidence is presented in Fig. 2 (f) operated under 10 % $H_2/N_2$, which is almost the same as the concentration produced during the DRM stage in the optimal tests (Fig. 2 (c)). Although the $H_2$ concentration achieved a notably high level for the DRM stage, the peak concentration of CO remained at a mere 0.5 %. This observation strongly suggests that in the DRM process, the predominant mechanism for CO production is the reverse Boudouard reaction involving carbon and $CO_2$, as opposed to the RWGS reaction. Therefore, the reaction between coke and $CO_2$ is believed to be the main source of CO yield in the presented ICCU-DRM process. Meanwhile, as shown in Fig. 2 (e), for CaO-$Ni/SiO_2$ (CaO followed by $Ni/SiO_2$), the CO concentration significantly increases compared to Fig. 2 (d), reaching a maximum of 2.0 %. This suggests that the $CO_2$ produced from the decomposition of $CaCO_3$ is interacting with coke, leading to further reactions.

$$CaCO_3 = CaO + CO_2 \qquad \text{Reaction (6)}$$

$$CH^* + CO_2 = CO_{gas} + H^* \qquad \text{Reaction (7)}$$

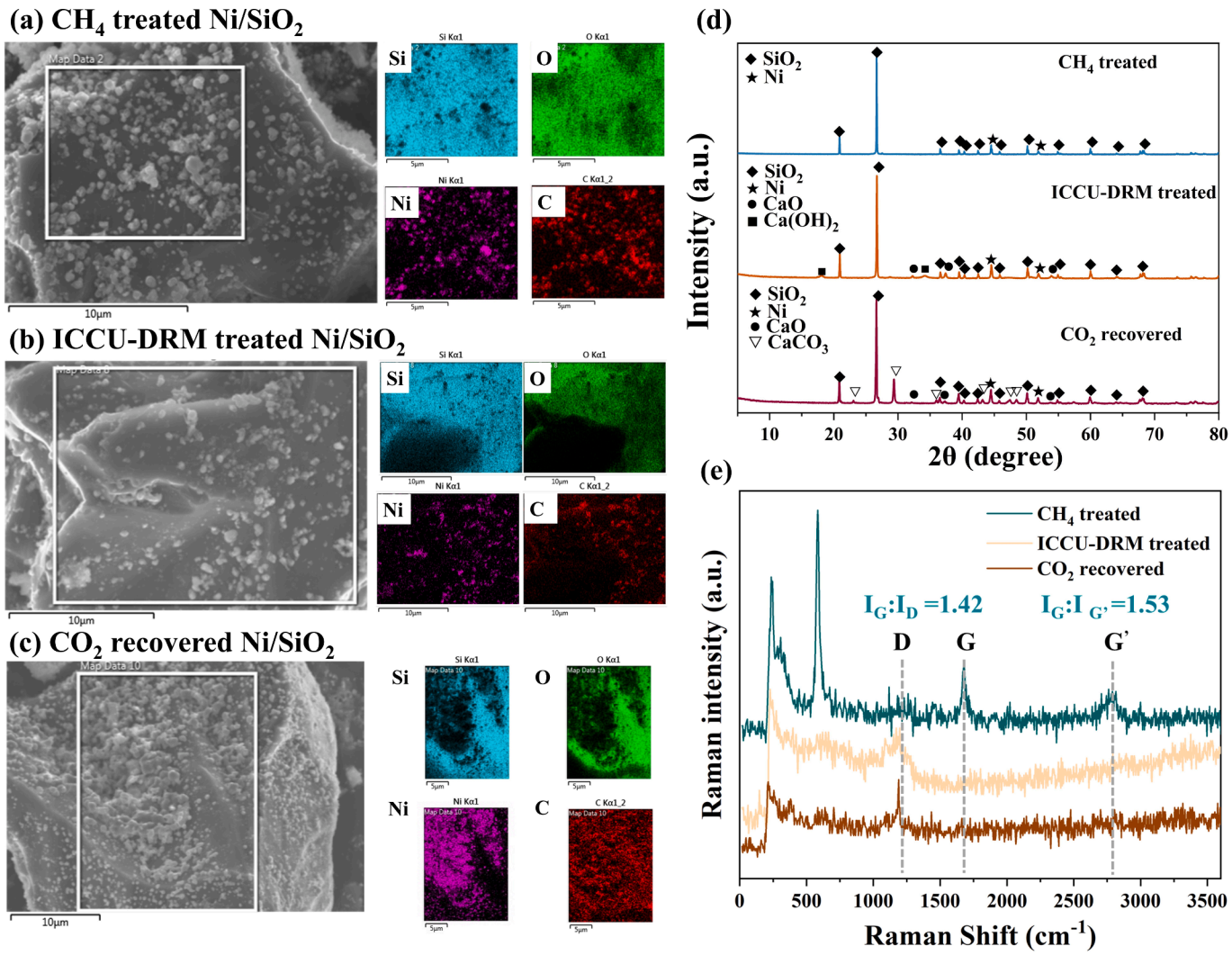


**Fig.4.** SEM images and EDX elemental mappings of the $Ni/SiO_2$ surface of: (a) $CH_4$ treated $Ni/SiO_2$ samples; (b) ICCU-DRM treated samples of $Ni/SiO_2$ and CaO mix and (c) $CO_2$ recovered samples of $Ni/SiO_2$ and $CaCO_3$ mix. (d) and (e) represent the XRD patterns and Raman spectra for the aforementioned samples, respectively.

$$C^* + CO_2 = 2CO_{gas} \qquad \text{Reaction (8)}$$

$$H_2 + CaCO_3 = CaO + CO_{gas} + H_2O \qquad \text{Reaction (9)}$$

As illustrated in Fig. 3, for $Ni/SiO_2$ & CaO, the yields of CO and $H_2$, as well as the uptake of $CO_2$ and $CO_2$ conversion, reach their highest levels. Specifically, these values are 43.41 mmol $g_{Ni/SiO_2}{}^{-1}$ for CO yield, 46.78 mmol $g_{Ni/SiO_2}{}^{-1}$ for $H_2$ yield, 17.39 mmol $g_{CaO}{}^{-1}$ for $CO_2$ uptake, and 87.2 % for $CO_2$ conversion, respectively. In the case of CaO-$Ni/SiO_2$, although the overall reaction rate is slower compared to the $Ni/SiO_2$ & CaO, the final yields and $CO_2$ conversion rate are quite similar. The respective values are 34.68 mmol $g_{Ni/SiO_2}{}^{-1}$ for CO yield, 53.98 mmol $g_{Ni/SiO_2}{}^{-1}$ for $H_2$ yield, 14.97 mmol $g_{CaO}{}^{-1}$ for $CO_2$ uptake, and 81.2 % for $CO_2$ conversion. In the case of $Ni/SiO_2$-CaO, a noticeable reduction in $CO_2$ conversion can be observed, dropping to only 20.1 %. Due to the inability of carbon deposits on the catalyst surface to be effectively cleared through the reaction with $CO_2$, the $H_2$ yield was also reduced [26], with only 27.34 mmol $g_{Ni/SiO_2}{}^{-1}$. Another observation of interest is related to $CO_2$ uptake. In scenarios where only CaO is used, as well as $Ni/SiO_2$-CaO, the $CO_2$ uptakes are comparable, ranging between 13–14 mmol $g_{CaO}{}^{-1}$. In contrast, for $Ni/SiO_2$ & CaO, the $CO_2$ uptake is akin to the scenario of $Ni/SiO_2$-CaO, with values hovering around 16–17 mmol $g_{CaO}{}^{-1}$. This is consistent with previous studies where metal materials were added to adsorbents, suggesting that the incorporation of Ni metal improves the $CO_2$ adsorption performance of CaO [49]. As Ni enhances the surface area of CaO and introducing new active sites favorable for adsorption. This synergy between Ni and CaO not only aids in more efficient $CO_2$ capture but also improves the thermal stability of CaO, preventing loss of adsorption capacity at high temperatures [50]. Integrating the results from Fig. 2 and Fig. 3, it is evident that $Ni/SiO_2$ & CaO yields the best outcome. Although the performance of $Ni/SiO_2$ & CaO and CaO-$Ni/SiO_2$ appear similar (as shown in Fig. 3), a comparison between Fig. 2 (c) and Fig. 2 (e) reveals that the $Ni/SiO_2$ & CaO combination favors an enhanced reaction rate, which presents a substantial advantage for practical applications. Therefore, we can confirm that the contact between the adsorbent and the catalyst plays a crucial role in accelerating the reaction rate, highlighting the significance of the interaction between adsorbents and catalysts in DFMs [51].

### 3.2. Analysis of coke on the $Ni/SiO_2$ catalyst

The above results from the decoupling test performance evaluation suggest that the reaction between the coke generated from $CH_4$ decomposition and $CO_2$ (i.e., the reverse Boudouard reaction (Reaction 8) is a significant approach for converting $CO_2$ in the ICCU-DRM process. Therefore, to further understand the reaction mechanism of ICCU-DRM, we have studied the coke using Raman spectroscopy as well as SEM and

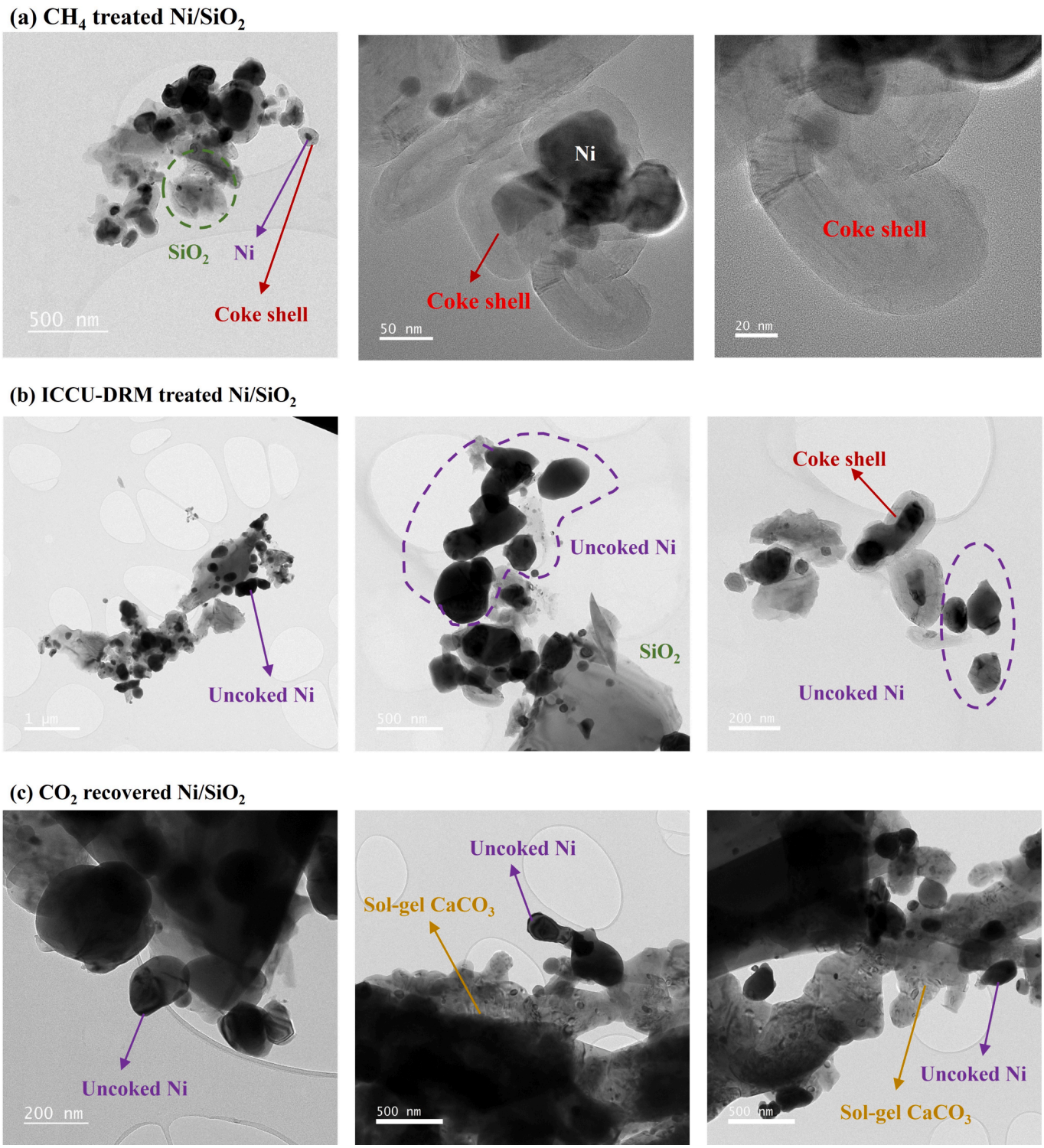


**Fig.5.** TEM images of (a) $CH_4$ treated $Ni/SiO_2$ samples; (b) ICCU-DRM treated samples of $Ni/SiO_2$ and CaO mix and (c) $CO_2$ recovered samples of $Ni/SiO_2$ and $CaCO_3$ mix.

TEM techniques. Fig. 4 (a) is the SEM images of $Ni/SiO_2$ after CH4 decomposition. Fig. 4 (b) and Fig. 4 (c) show the SEM images of $Ni/SiO_2$ & CaO after ICCU-DRM and the subsequent $CO_2$ treatments, respectively. It is observed that the distribution of carbon (C) elements closely resembles that of nickel (Ni), indicating that Ni metal plays a crucial role in splitting $CH_4$ to produce coke. In examining the surface of the sample displayed in Fig. 4 (c), which originated from Fig. 4 (b) but underwent a $CO_2$ treatment aimed at gasifying the coke, it is notable that carbon elements are still detectable across the entire surface. Theoretically, post-$CO_2$ treatment, the surface is expected to be free of coke, as per reference [52]. Yet, carbon presence is evident, differing from the samples in Fig. 4 (a) and Fig. 4 (b), where the carbon was primarily on the Ni surface. Here, it is uniformly distributed over the entire $Ni/SiO_2$ surface. If the SEM results presented in Fig. 4 (c) are accurate, it is highly probable that the observed carbon element primarily derives from the adsorption of $CO_2$ rather than from coke. This inference is supported by

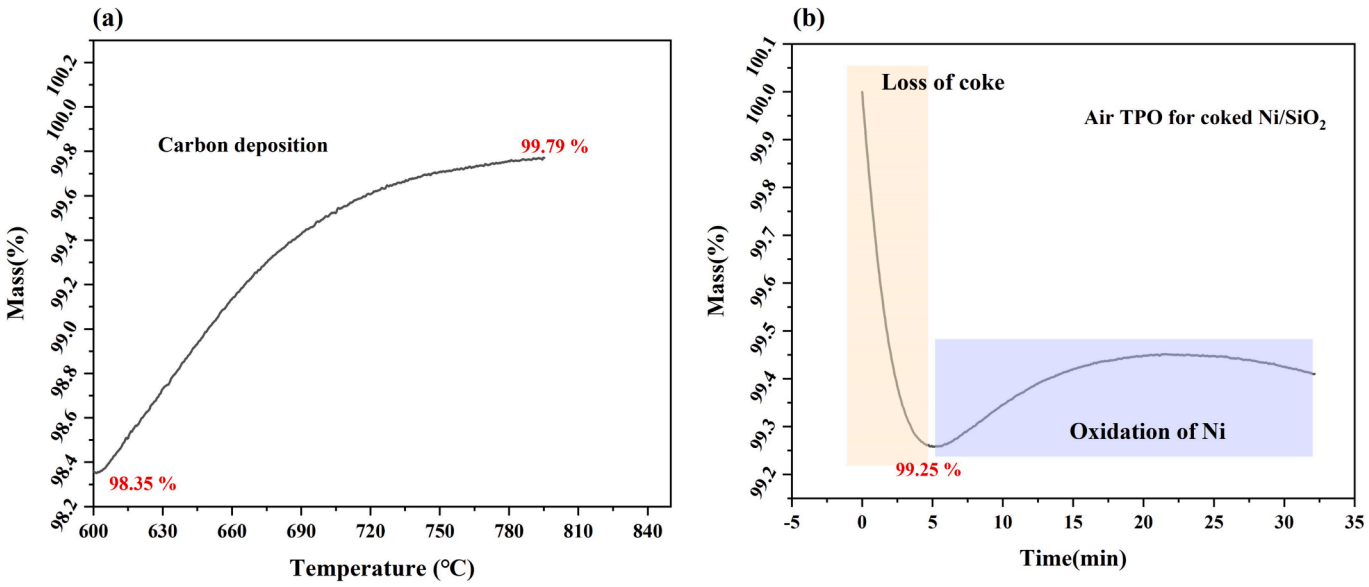


**Fig.6.** (a) Mass change of $Ni/SiO_2$ in a 10% $CH_4/N_2$ environment between 600–850 °C; (b) Mass change of coked $Ni/SiO_2$ under constant temperature of 650 °C in air.

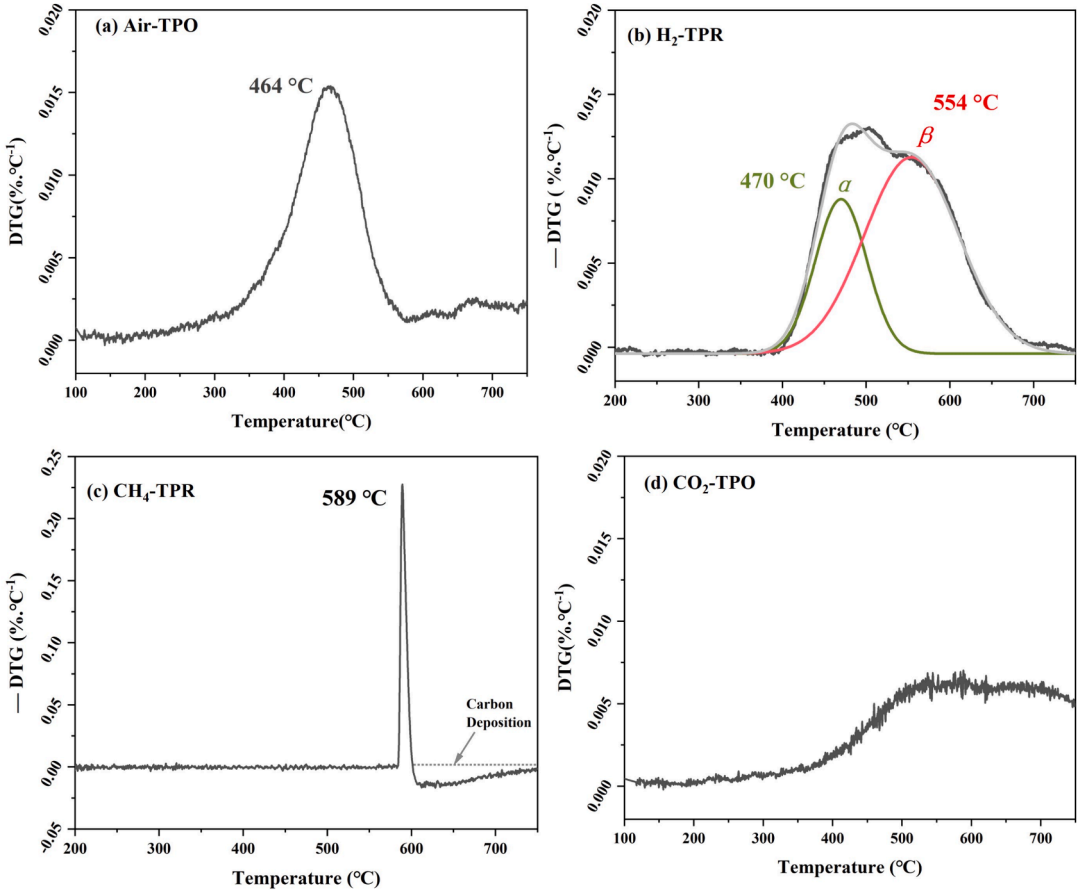


**Fig.7.** DTG (% $°C^{-1}$) pattern of TGA tests of (a) air–TPO test for reduced $Ni/SiO_2$, (b) $H_2$-TPR test for $NiO/SiO_2$, (c) $CH_4$–TPR test for $NiO/SiO_2$, and (d) $CO_2$–TPO test for reduced $Ni/SiO_2$.

the notion that $CO_2$ can react with and substantially consume coke (reverse Boudouard reaction). This reaction occurs so readily on Ni metal surfaces that it is almost impossible for coke to remain unreacted in the presence of $CO_2$ [34,53,54]. Therefore, under typical conditions, coked DFMs treated by $CO_2$ are unlikely to have any coke. On the other hand, if the carbon were attributable to coke, its distribution would likely coincide mainly with that of Ni elements like in Fig. 4 (a) and Fig. 4 (b), rather than being uniformly dispersed across the $Ni/SiO_2$

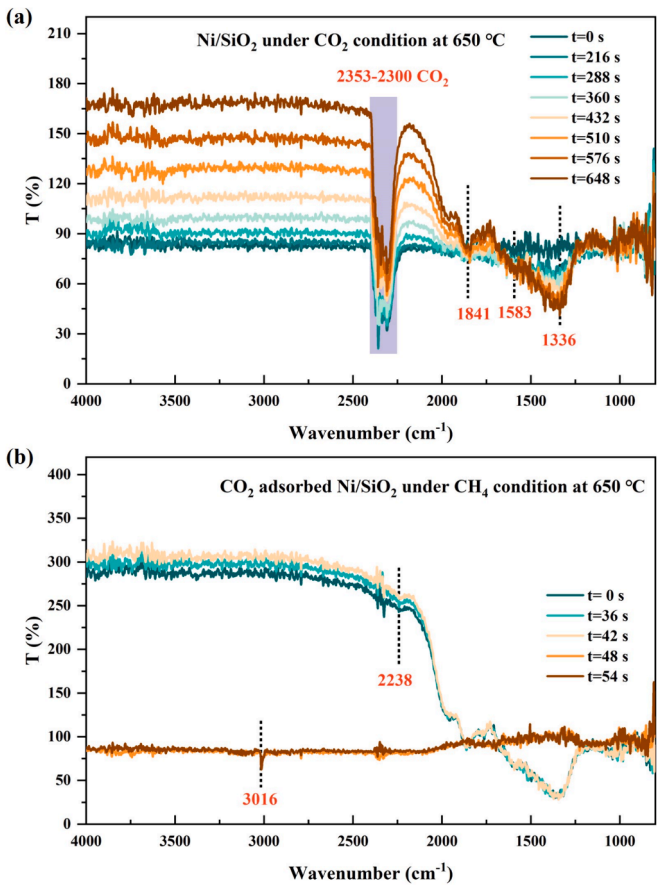


**Fig.8.** In-situ DRIFTS of $Ni/SiO_2$ during $CO_2$ capture stage (a) and the following $CH_4$ recover stage (b) at 650 °C.

surface. Thus, we suppose that $CO_2$ could be attached to the surface of $Ni/SiO_2$. This phenomenon is quite intriguing, and we will discuss it further in subsequent sections on $CO_2$-TPO and in situ DRIFT tests. Fig. 4 (d) and Fig. 4 (e) represent the XRD and Raman spectra of the three samples, respectively. The related SEM and EDX results are shown in Fig. 4 (a), Fig. 4(b) and Fig. 4 (c). In all samples presented in Fig. 4 (d), distinct peaks of Ni and $SiO_2$ are observable. Notably, in the sample treated with ICCU-DRM, peaks associated with $Ca(OH)_2$ can be observed. Therefore, the $H_2O$ produced from the DRM reaction could be combined with CaO [55]. For the samples after $CO_2$ adsorption, it is observed the coexistence of peaks for CaO and $CaCO_3$, suggesting an incomplete adsorption of $CO_2$ for CaO. Due to the inability of XRD testing to detect peaks associated with coke, we additionally conducted Raman analysis on these three samples. However, in the Raman analysis, we observed the three characteristic peaks of coke only in the first set of samples, which underwent $CH_4$ decomposition. These peaks are the D—bond (~1350 $cm^{-1}$), G—bond (~1580 $cm^{-1}$), and G'—bond (~2700 $cm^{-1}$)[34]. It is suggested that in the second and third sets of samples, the involvement of $CO_2$ in the reaction significantly consumed the coke deposition. The absence of peaks related to coke further suggests that the carbon element observed in Fig. 4 (c) primarily originates from the adsorption of $CO_2$. The residual coke might be either too small in size or too low in orderness [56]. The D to G band ratio is often used to evaluate the degree of disorder in carbon materials, while the G to G' band ratio is indicative of the graphitisation level of carbon materials [57,58]. For the $Ni/SiO_2$ after $CH_4$ decomposition, it is observed that the intensity ratio of the G to D bond and the G to G' bond both exceeded 1, being 1.42 and 1.35, respectively. Therefore, the coke resulting from the catalytic pyrolysis of $CH_4$ by $Ni/SiO_2$ possesses a higher degree of order and fewer defects [57].

Furthermore, it is noteworthy that the Ni particles on the $SiO_2$ surface in Fig. 4 (a) appear to be larger compared to those in Fig. 4 (b) and (c). This may be due to their encapsulation by the coke. TEM images corroborate this hypothesis. In the TEM image, the dark spots represent Ni metal, while the semi-transparent shells enveloping the Ni indicate coke. The large, semi-transparent objects are $SiO_2$. The darker, but not completely black, large chunks with rounded edges are identified as sol–gel CaO. As shown in Fig. 5 (a), for the coked–$Ni/SiO_2$ samples prepared after $CH_4$ decomposition, Ni metal particles are encapsulated by a semi-transparent coke film. This form of coke has also been reported in some literature elsewhere [59]. Importantly, our previous research revealed that the coke produced on Ni/CaO DFM during the ICCU-DRM process predominantly exists in the form of carbon nanotubes [31,34]. This seems to suggest that the type of support for the Ni catalyst has an influence on the morphological formation of the coke. In Fig. 5 (b), observing Ni metal particles unencapsulated by a coke shell reveals $CaCO_3$ actively participates in coke consumption. Furthermore, in Fig. 5 (c), the near absence of coke shells suggests that $CO_2$ is effective in removing coke. These findings indicate that the reverse Boudouard reaction (Reaction 8) plays a significant role in reducing coke during the ICCU-DRM process, thereby contributing to the regeneration of active sites on the catalyst surface [60,61].

To estimate the content of coke, TGA tests were conducted on $Ni/SiO_2$, as shown in Fig. 6 (a). In the temperature range of 600–850 °C under a 10 % $CH_4/N_2$ environment, the mass percentage of $Ni/SiO_2$ reduced by 5 % $H_2$/Ar, increased from 98.35 % to 99.79 %, tending towards saturation with a mass change rate of 1.46 %. This suggests that coke could cause a 1.46 % increase in the $Ni/SiO_2$ mass. Furthermore, as illustrated in Fig. 6 (b), the mass of coked $Ni/SiO_2$ in air, under a constant temperature of 650 °C, decreased from 100 % to a minimum of 99.25 %. This mass loss is attributable to the oxidation of coke. However, it is noted that in an $O_2$-contained environment, Ni might also be oxidized, leading to an increase in mass. This process occurs concurrently with the consumption of coke. Therefore, the actual mass loss due to coke oxidation might be higher. Thus, it is estimated that the content of coke for the $Ni/SiO_2$ catalyst used in this experiment ranges between 0.75 % and 1.46 %.

### 3.3. *Reaction pathway investigation*

There exists a possibility that although $Ni/SiO_2$ is designed for catalysis, it might have an impact on the adsorption process because of its surface activity. Similarly, for $CaO/CaCO_3$, even though its primary purpose is set for adsorption of $CO_2$, its influence on the catalysis process is also worth exploring. Therefore, it is necessary to explore the behavior of $Ni/SiO_2$ under $CO_2$ environments and also that of $CaO/CaCO_3$ under $CH_4$ environments, to better understand the interplay between the catalyst and adsorbent on the DFMs during ICCU-DRM.

As illustrated in Fig. 7 (a), it can be observed that in air, the oxidation of $Ni/SiO_2$ reaches its maximum at approximately 464 °C. This indicates that the oxidation reaction of Ni metal intensifies at this temperature. As depicted in Fig. 7 (b), for the oxidised $NiO/SiO_2$, two distinct peaks are observed during the reduction in 5 % $H_2$/Ar, occurring at approximately 470 °C and 554 °C. The peak at 470 °C corresponds to the reduction of free NiO, while the peak at 554 °C is attributed to the reduction of interacted NiO, indicating the formation of nickel silicate with the $SiO_2$ support, which requires a higher temperature for reduction [62]. As illustrated in Fig. 7 (c), during $CH_4$-TPR, a notable difference from $H_2$-TPR is observed. No reaction occurred between the oxidised $NiO/SiO_2$ and $CH_4$ until 580 °C. However, almost instantaneously, at 589 °C, a sharp peak emerges, signifying a rapid reduction. This phenomenon aligns with our previous research finding that the reduction of NiO by $CH_4$ requires initial penetration through the oxide layer of NiO [34]. Subsequently, the DTG value shifts from negative to positive, suggesting an increase in mass, which should be attributed to carbon deposition. More importantly, for the $CO_2$-TPO test of $Ni/SiO_2$, as shown in Fig. 7

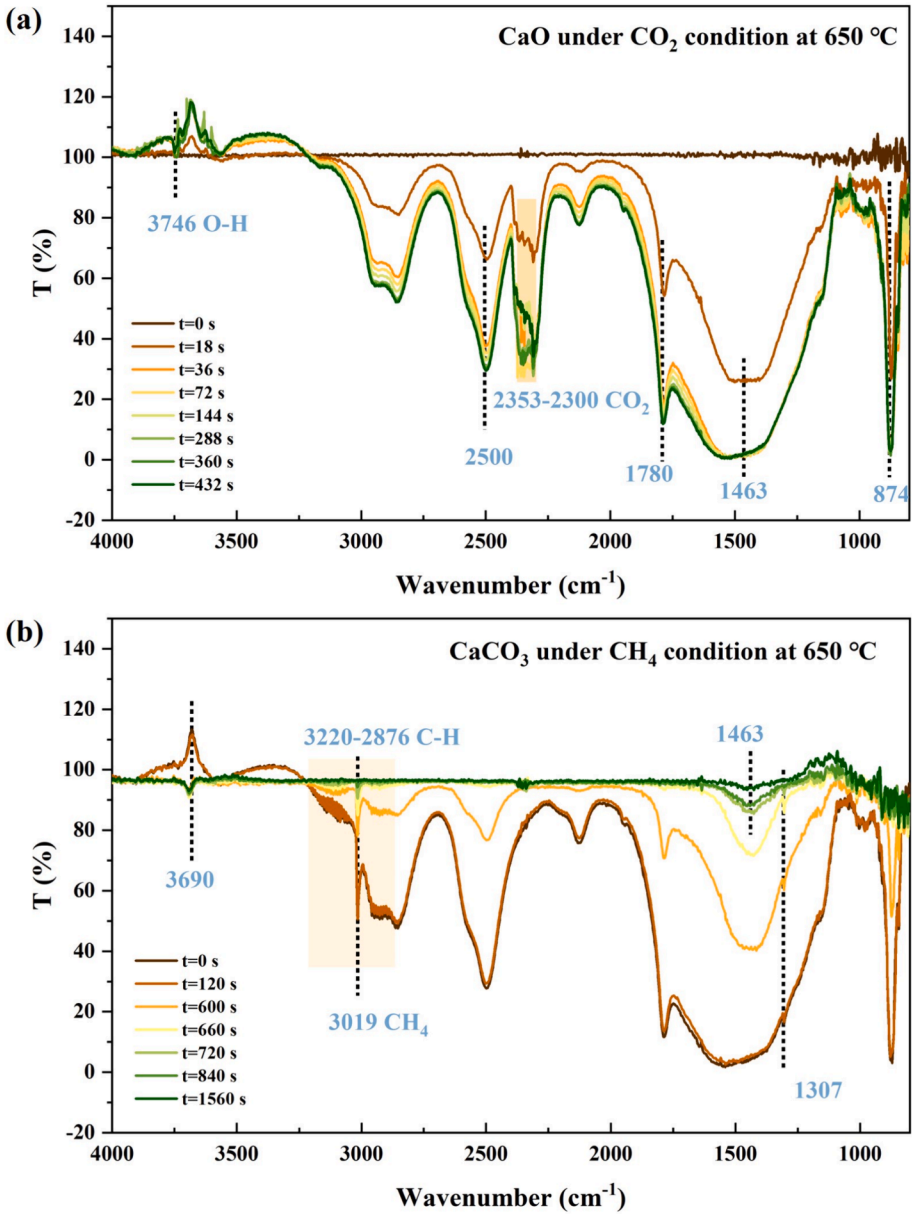


**Fig.9.** In-situ DRIFTS of CaO during $CO_2$ capture stage (a) and the following $CH_4$ recover stage (b) at 650 °C.

(d), a gradual increase in the DTG value begins at approximately 400 °C, the value eventually stabilising around 0.005 % $°C^{-1}$. The mass increase of $Ni/SiO_2$ in a $CO_2$ environment corroborates the possibility, mentioned earlier, that $Ni/SiO_2$ inherently possesses the capacity to adsorb $CO_2$. Since the adsorption took place at around 400 °C, it was unlikely to be physical adsorption but more likely to be chemical adsorption [63].

Through conducting DRIFTS tests, we further investigated the reaction between $Ni/SiO_2$ and $CO_2$, as shown in Fig. 8. As demonstrated in Fig. 8 (a), peaks from 2353 $cm^{-1}$ to 2300 $cm^{-1}$ represent $CO_2$. Meanwhile, carbonate peaks appear at 1336 $cm^{-1}$, 1583 $cm^{-1}$ and 1841 $cm^{-1}$ on $Ni/SiO_2$ under a $CO_2$ environment [64]. This suggests that $CO_2$ can be chemisorbed on the $Ni/SiO_2$ catalyst, which would be advantageous for the reaction between $CO_2$ and coke for DRM [24,25]. The adsorption mechanism leading to the formation of carbonate-like structures could stem from adsorption of $CO_2$ by $SiO_2$ [65]. On the other hand, it might also be attributed to Ni. As Ni is a transition metal with unfilled d-orbitals, easily forms chemical bonds by accepting or providing electrons for more stable configurations, granting it strong surface activity and the ability to adsorb various chemicals on its surface. In fact, numerous studies have demonstrated that the adsorption of $CO_2$ on the surface of Ni metal plays a crucial role in the catalysis of the DRM process [66,67]. During the $CH_4$ reduction stage (Fig. 8 (b)), it is found that the various peaks rapidly revert to their initial state within 1 min, indicating a swift reaction between $CH_4$ and the adsorbed $CO_2$. The peak at 2238 $cm^{-1}$ represents C—O [68], which means the formation of CO. While the peak at 3016 $cm^{-1}$ represents $CH_4$.

DRIFTS tests were also conducted on CaO under the same conditions. Fig. 9 (a) illustrates the process of CaO adsorbing $CO_2$, while Fig. 9 (b) depicts the reduction process of the adsorbed $CaCO_3$ in a $CH_4$ environment. As shown in Fig. 9 (a), peaks at 874 $cm^{-1}$,1463 $cm^{-1}$,1780 $cm^{-1}$ and 2500 $cm^{-1}$ can be attributed to carbonate caused by the formation of $CaCO_3$ [69]. Compared to the $CO_2$ adsorption stage, no new peaks appear during the CH4 reduction stage, as demonstrated by Fig. 9 (b), aside from the peaks related to $CH_4$ (3220 $cm^{-1}$-2876 $cm^{-1}$). This indicates that $CH_4$ hardly reacts with $CaCO_3$, and the reduction of $CaCO_3$ in a $CH_4$ environment is primarily due to its own thermal decomposition, as the situation is shown in Fig. 2 (b). Furthermore, the peak at 1463 $cm^{-1}$ can be attributed to the incomplete decomposition of $CaCO_3$ [69],

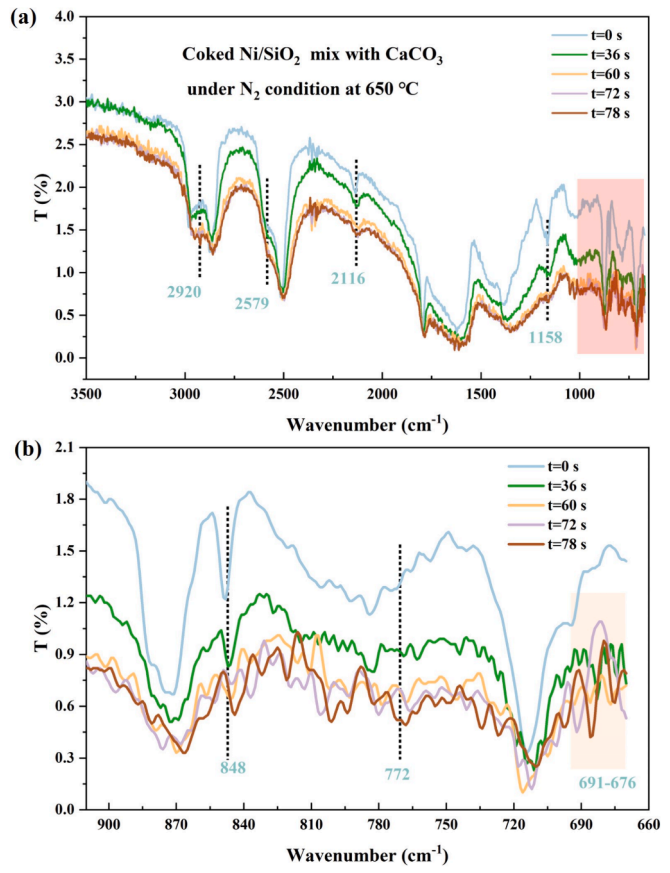


**Fig.10.** In-situ DRIFTS of coked Ni/$SiO_2$ mix with $CaCO_3$ under $N_2$ condition at 650 °C with wavenumbers ranging from 680 to 3500 $cm^{-1}$(a) and detailed information in the range from 680 to 900 $cm^{-1}$(b).

resulting in the residual carbonate groups. Meanwhile, the peak at 3746 $cm^{-1}$, representing O—H, could be a product of the interaction between hydrogen atoms from the $CH_4$ and oxygen atoms on CaO [70].

Fig. 10 presents the results of in situ DRIFTS tests conducted on a mixture of $CaCO_3$ and coked Ni/$SiO_2$ under a $N_2$ atmosphere at 650 °C. Fig. 10 (a) shows the full spectrum, while Fig. 10 (b) displays a detailed spectrum ranging from 900 $cm^{-1}$ to 680 $cm^{-1}$. The peaks in Fig. 10 (a) at 1158 $cm^{-1}$ and 2116 $cm^{-1}$ correspond to the C—O bonds formed by the combination of carbon elements in coke and oxygen elements in $CaCO_3$ [71]. The rapid decline of these two peaks after 78 s from the start of the reaction suggests that the reverse Boudouard reaction between coked Ni/$SiO_2$ and $CaCO_3$ occurs rapidly [72]. This observation is consistent with some studies on the reaction mechanisms of DRM [25–27]. The peak at 2579 $cm^{-1}$ corresponds to the C—H bond. The intensity of this peak gradually increases with the progress of the reaction, indicating the ongoing dehydrogenation of incompletely dehydrogenated $CH_2$ or $CH_3$ groups in the coke, progressively forming C—H. As the dehydrogenation proceeds, substances with C—H single bonds are formed. This is corroborated by the gradual weakening of the peak at 848 $cm^{-1}$, which represents C—$H_2$ [73]. This trend becomes most pronounced at t = 72 s, revealing that while C—H is being generated, C—$H_2$ is diminishing, corresponding precisely to the dehydrogenation of C—$H_2$. Simultaneously, the peak at 2920 $cm^{-1}$ appears, representing the asymmetric stretching vibration of the C—H bond. This manifests that C—$H_2$ or C—$H_3$ groups are being activated on the surface of the Ni [74], suggesting the presence of partially dehydrogenated C—$H_2$ or C—$H_3$ in the coke.

At the same time, the peak intensity at 772 $cm^{-1}$ gradually increases, representing the O—H group [75]. It reveals the presence of a reaction pathway involving O—H as an intermediate product in the reaction between $CO_2$ and coke. Such a reaction pathway has also been reported in previous studies [24], as illustrated in Reaction 10 and Reaction 11. Also, significant fluctuations are observed in the peak between 691 and 676 $cm^{-1}$, representing the Si—O—Si bond [76]. This suggests that $SiO_2$, serving as the support, also plays a role in the reaction. The reason might be related to the adsorption of $CO_2$ on the Ni/$SiO_2$ catalyst, as mentioned from the SEM analysis (Fig. 4 (c)), the $CO_2$–TPO (Fig. 7 (d)) test and the In-situ DRIFTS test (Fig. 8) in this section. The results could show that the catalyst plays a crucial role in facilitating the reverse Boudouard reaction.

$$CH^* + O^* = CHO^* \quad \text{Reaction (10)}$$

$$CHO^* = CO\,(gas) + H^* \quad \text{Reaction (11)}$$

As demonstrated in Fig. 11 (a), a calculation of adsorption energies reveals that $CO_2$ exhibits adsorption energy of 0.02 eV on Ni surfaces, while on CaO, the value is −0.02 eV. This suggests that $CO_2$ adsorption on CaO is a spontaneous process, whereas Ni shows relatively weaker adsorption capabilities for $CO_2$. Considering solely the capacity to adsorb $CO_2$, CaO seems to be more effective in facilitating the reaction between $CO_2$ and coke. Also, given that $H_2$ can directly react with $CaCO_3$, it is plausible that coke, as a reductive solid, also has the potential to directly engage in a reaction with $CaCO_3$ [7,33]. Therefore, the exploration into whether the reverse Boudouard reaction predominantly occurs on the surface of CaO or Ni/$SiO_2$ surfaces is thus significant. The DFT analysis shown in Fig. 11 (b) illustrates that the activation energy required for the reverse Boudouard reaction on Ni (1 1 1) surfaces is lower than that on CaO (0 0 1) surfaces, indicating a preference for this reaction to occur on Ni surfaces. Based on this, to further investigate the potential possibility and reaction efficiency between $CaCO_3$ and coke in the absence of a catalyst, we mixed $CaCO_3$ with graphene to study the CO yield under catalyst-free conditions. In Fig. 11 (c), direct heating of a $CaCO_3$ and graphene mixture shows a peak $CO_2$ concentration of 0.61 %, significantly higher than that of CO (below 0.10 %). The results indicate that without Ni/$SiO_2$, it is challenging for $CaCO_3$ alone to directly engage in the reverse Boudouard reaction with carbon. It implies that in the ICCU-DRM process, the reaction between coke and $CO_2$ should primarily rely on the presence of Ni/$SiO_2$. To explore if direct contact between $CaCO_3$ and coked Ni/$SiO_2$ improves the reverse Boudouard reaction efficiency, we analyzed CO production at 650 °C in an $N_2$ environment, comparing conditions where $CaCO_3$ was either in direct contact with coked Ni/$SiO_2$ ($CaCO_3$ & coked Ni/$SiO_2$) or not ($CaCO_3$-coked Ni/$SiO_2$). As shown in Fig. 11 (d), for $CaCO_3$-coked Ni/$SiO_2$, the peak CO concentration reaches 0.82 %, with the reaction completing around 11500 s. In contrast, for $CaCO_3$ & coked Ni/$SiO_2$, the peak CO concentration reaches 1.80 %, and the reaction concludes within 5000 s. It reveals that, despite CaO/$CaCO_3$ having almost no catalytic function for the reverse Boudouard reaction during the ICCU-DRM process, direct contact between $CaCO_3$ and coked Ni/$SiO_2$ is more conducive to $CO_2$ conversion. Therefore, a closer integration of adsorbents and catalysts within DMFs should benefit their performance enhancement. This underscores the importance of the coordinated interaction between adsorbents and catalysts again [31].

Based on the aforementioned analyses, the reaction mechanism of ICCU-DRM is illustrated in Fig. 12. During the $CO_2$ capture stage, CaO acts as an adsorbent, sequestering a significant amount of $CO_2$ to form $CaCO_3$. In the DRM phase, the catalyst plays a pivotal role. On the one hand, it is responsible for the dehydration of $CH_4$, producing $H_2$ and the coke on its surface. On the other hand, Ni/$SiO_2$ is capable of adsorbing a minimal quantity of $CO_2$, which is instrumental in facilitating the reaction between $CO_2$ and the formed coke, thereby catalysing the reverse Boudouard reaction for the conversion of $CO_2$. Meanwhile, $CaCO_3$ mainly functions in the release of $CO_2$ gas. It is imperative to note that the reverse Boudouard reaction should occur on the surface of the catalyst.

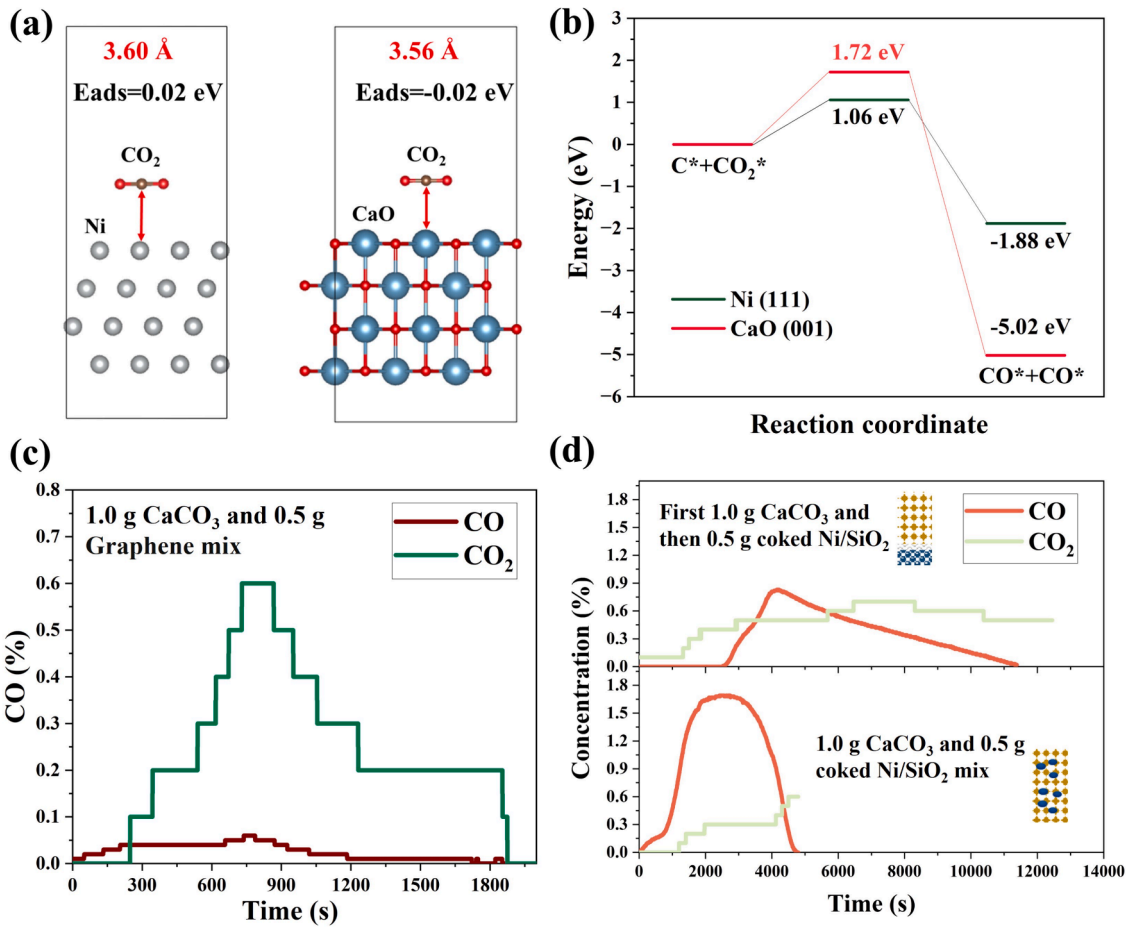


**Fig.11.** (a): DFT analysis of $CO_2$ adsorption energies on Ni surfaces and CaO Surfaces. (b): DFT alculation of activation energies for the reverse Boudouard reaction on Ni Catalyst and CaO surfaces. (c): Concentration Curves of CO and $CO_2$ for the Reaction of 1.0 g of $CaCO_3$ and 0.5 g mix of Graphene at 650 °C in a 100 mL.min$^{-1}$ $N_2$ flow. (d): Comparative concentration curves of CO and $CO_2$ for 1.0 g of $CaCO_3$ reacted with 0.5 g of coked-Ni/$SiO_2$, in sequential addition and uniform mixing approaches at the same temperature and $N_2$ flow conditions.

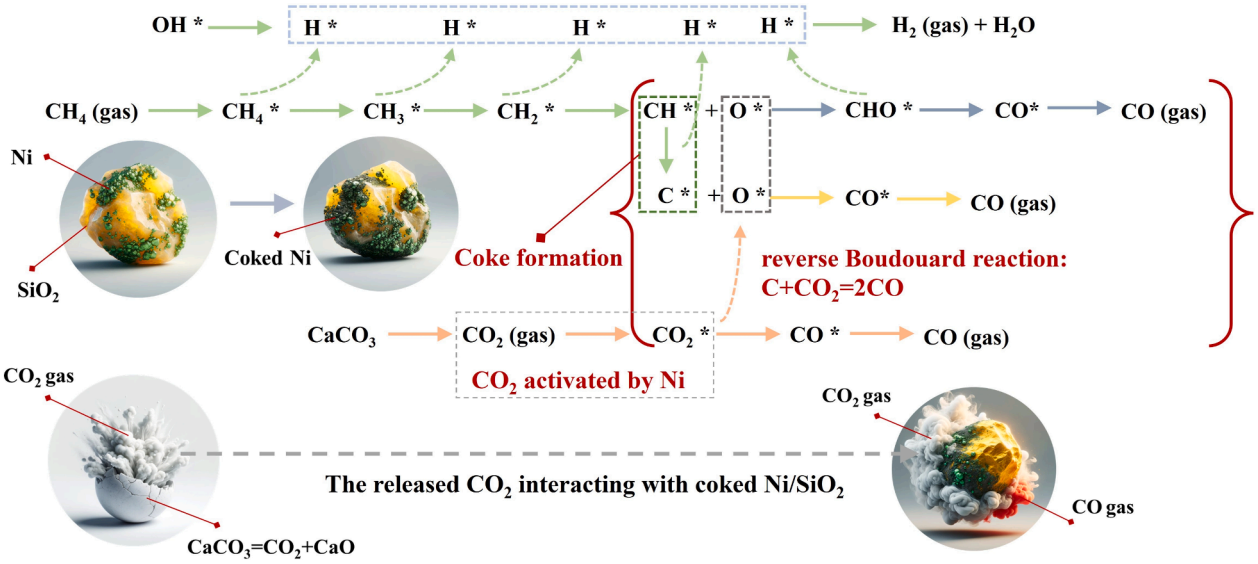


**Fig.12.** Schematic diagram of the ICCU-DRM reaction pathways.

## 4. Conclusions

This study evaluated the roles of Ni/$SiO_2$ catalyst and sol–gel synthesised CaO sorbent in ICCU-DRM using a decoupling approach, exploring the interaction mechanisms between catalyst and sorbent to provide guidance for designing more efficient DFMs. The key findings

are as follows:

(1) Through decoupling experiments, it was revealed that $Ni/SiO_2$ catalyst facilitates $CH_4$ dehydrogenation to produce coke and $H_2$, with maximal yields of 43.41 mmol $g^{-1}$ for CO and 46.78 mmol $g^{-1}$ for $H_2$. The reverse Boudouard reaction on the $Ni/SiO_2$ surface is vital for $CO_2$ conversion up to 87.2 %.

(2) Characterisations via SEM, TEM and Raman spectroscopy verify that coke encapsulating Ni nanoparticles react with $CO_2$, indicating the necessity of sufficient contact between catalyst and sorbent.

(3) In-situ DRIFTS proves that while no obvious reaction occurs between $CaCO_3$ and $CH_4$, and $CO_2$ chemisorption on $Ni/SiO_2$ enables the reverse Boudouard reaction. DFT calculations further reveal that Ni surfaces promote this reaction with a lower activation energy barrier than CaO.

Therefore, intimate mixing contact between $Ni/SiO_2$ and CaO is crucial for excellent DRM performance through synergistic effects, where $Ni/SiO_2$ activates $CO_2$ to react with coke while CaO captures $CO_2$ from exhaust gas and then supplies $CO_2$ during DRM. Further insights into interfacial interactions between catalyst and sorbent components are vital for optimising dual-functional materials design.

## CRediT authorship contribution statement

**Xiaotong Zhao:** Writing – original draft, Methodology, Investigation, Formal analysis, Conceptualization. **Shuzhuang Sun:** Methodology, Formal analysis, Data curation, Conceptualization. **Yuanyuan Wang:** Investigation, Formal analysis. **Yingrui Zhang:** Methodology, Investigation, Formal analysis. **Yuan Zhu:** Investigation, Formal analysis, Data curation. **Bo Zong:** Investigation, Formal analysis, Data curation. **Jia Hu:** Investigation, Formal analysis, Data curation. **Paul Williams:** Writing – review & editing, Methodology, Investigation, Formal analysis. **Chunfei Wu:** Writing – review & editing, Supervision, Methodology, Investigation, Formal analysis, Data curation, Conceptualization.

## Declaration of competing interest

The authors declare that they have no known competing financial interests or personal relationships that could have appeared to influence the work reported in this paper.

## Data availability

The authors are unable or have chosen not to specify which data has been used.

## Acknowledgements

This project has received funding from the European Union's Horizon 2020 research and innovation programme under grant agreement No 872102.

## References

[1] D.I. Armstrong McKay, A. Staal, J.F. Abrams, R. Winkelmann, B. Sakschewski, S. Loriani, I. Fetzer, S.E. Cornell, J. Rockström, T.M. Lenton, Exceeding 1.5 °C global warming could trigger multiple climate tipping points, Science 377 (6611) (2022) eabn7950, https://doi.org/10.1126/science.abn7950.

[2] Y. Qiao, W. Liu, R. Guo, S. Sun, S. Zhang, J.J. Bailey, M. Fang, C. Wu, Techno-economic analysis of integrated carbon capture and utilisation compared with carbon capture and utilisation with syngas production, Fuel 332 (2023) 125972, https://doi.org/10.1016/j.fuel.2022.125972.

[3] J. Chen, Y. Xu, P. Liao, H. Wang, H. Zhou, Recent progress in integrated $CO_2$ capture and conversion process using dual function materials: a state-of-the-art review, Carbon Capture Sci. Technol. 4 (2022) 100052, https://doi.org/10.1016/j.ccst.2022.100052.

[4] D.Y.C. Leung, G. Caramanna, M.M. Maroto-Valer, An overview of current status of carbon dioxide capture and storage technologies, Renew. Sustain. Energy Rev. 39 (2014) 426–443, https://doi.org/10.1016/j.rser.2014.07.093.

[5] L. Yang, J. Heinlein, C. Hua, R. Gao, S. Hu, L. Pfefferle, Y. He, Emerging dual-functional 2D transition metal oxides for carbon capture and utilization: a review, Fuel 324 (2022) 124706, https://doi.org/10.1016/j.fuel.2022.124706.

[6] D. González-Varela, C. Hernández-Fontes, N. Wang, H. Pfeiffer, State of the art and perspectives of the $CO_2$ chemisorption in ceramics with its simultaneous or subsequent chemical transformation, Carbon Capture Sci. Technol. 7 (2023) 100101, https://doi.org/10.1016/j.ccst.2023.100101.

[7] S. Sun, Y. Wang, X. Zhao, C. Zhang, C. Wu, One step upcycling $CO_2$ from flue gas into CO using natural stone in an integrated $CO_2$ capture and utilisation system, Carbon Capture Sci. Technol. 5 (2022) 100078, https://doi.org/10.1016/j.ccst.2022.100078.

[8] Y. Guo, J. Sun, R. Wang, W. Li, C. Zhao, C. Li, J. Zhang, Recent advances in potassium-based adsorbents for $CO_2$ capture and separation: a review, Carbon Capture Sci. Technol. 1 (2021) 100011, https://doi.org/10.1016/j.ccst.2021.100011.

[9] Z. Lv, S. Chen, X. Huang, C. Qin, Recent progress and perspective on integrated $CO_2$ capture and utilization, Curr. Opin. Green Sustainable Chem. 40 (2023) 100771, https://doi.org/10.1016/j.cogsc.2023.100771.

[10] H. Ishaq, I. Dincer, C. Crawford, A review on hydrogen production and utilization: challenges and opportunities, Int. J. Hydrogen Energy 47 (62) (2022) 26238–26264, https://doi.org/10.1016/j.ijhydene.2021.11.149.

[11] S. Masoudi Soltani, A. Lahiri, H. Bahzad, P. Clough, M. Gorbounov, Y. Yan, Sorption-enhanced steam methane reforming for combined $CO_2$ capture and hydrogen production: a state-of-the-art review, Carbon Capture Sci. Technol. 1 (2021) 100003, https://doi.org/10.1016/j.ccst.2021.100003.

[12] R. Chen, G.M. Weng, Sustainable energy resources for driving methane conversion, Adv. Energy Mater. 13 (36) (2023) 2301734, https://doi.org/10.1002/aenm.202301734.

[13] H. Pan, X. Zheng, R. Wu, X. Liu, S. Xiao, L. Sun, T. Hu, Z. Gao, L. Yang, C. Huang, X. Zhang, S. Deng, Y. Xiao, Agriculture related methane emissions embodied in China's interprovincial trade, Renew. Sustain. Energy Rev. 189 (2024) 113850, https://doi.org/10.1016/j.rser.2023.113850.

[14] E. Workie, V. Kumar, A. Bhatnagar, Y. He, Y. Dai, Y. Wah Tong, Y. Peng, J. Zhang, C. Fu, Advancing the bioconversion process of food waste into methane: a systematic review, Waste Management 156 (2023) 187–197, https://doi.org/10.1016/j.wasman.2022.11.030.

[15] S.G. Nnabuife, J. Ugbeh-Johnson, N.E. Okeke, C. Ogbonnaya, Present and projected developments in hydrogen production: a technological review*, Carbon Capture Sci. Technol. 3 (2022) 100042 https://doi.org/10.1016/j.ccst.2022.100042.

[16] G. Liu, S. Sun, H. Sun, Y. Zhang, J. Lv, Y. Wang, J. Zeng, Z. Yan, C. Wu, Integrated $CO_2$ capture and utilisation: a promising step contributing to carbon neutrality, Carbon Capture Sci. Technol. 7 (2023) 100116, https://doi.org/10.1016/j.ccst.2023.100116.

[17] S. Sun, H. Sun, P.T. Williams, C. Wu, Recent advances in integrated $CO_2$ capture and utilization: a review, Sustainable Energy Fuels 5 (18) (2021) 4546–4559, https://doi.org/10.1039/d1se00797a.

[18] A. Nawar, H. Ghaedi, M. Ali, M. Zhao, N. Iqbal, R. Khan, Recycling waste-derived marble powder for $CO_2$ capture, Process Saf. Environ. Prot. 132 (2019) 214–225, https://doi.org/10.1016/j.psep.2019.10.005.

[19] S. Sun, C. Zhang, S. Chen, X. Zhao, Y. Wang, S. Xu, C. Wu, Integrated $CO_2$ capture and reverse water–gas shift reaction over $CeO_2$-CaO dual functional materials, Royal Soc. Open Sci. 10 (4) (2023) 230067.

[20] J. Wu, Y. Zheng, J. Fu, Y. Guo, J. Yu, J. Chu, P. Huang, C. Zhao, Synthetic Ni–CaO–$CeO_2$ dual function materials for integrated $CO_2$ capture and conversion via reverse water–gas shift reaction, Sep. Purif. Technol. 317 (2023) 123916, https://doi.org/10.1016/j.seppur.2023.123916.

[21] A.M. Alhassan, I. Hussain, O.A. Taialla, M.M. Awad, A. Tanimu, K. Alhooshani, S. A. Ganiyu, Advances in catalytic dry reforming of methane (DRM): Emerging trends, current challenges, and future perspectives, J. Clean. Prod. 423 (2023) 138638, https://doi.org/10.1016/j.jclepro.2023.138638.

[22] X. Wang, S. Xu, W. Yang, X. Fan, Q. Pan, H. Chen, Development of Ni-Co supported on SBA-15 catalysts for non-thermal plasma assisted co-conversion of CO2 and CH4: Results and lessons learnt, Carbon Capture Sci. Technol. 5 (2022) 100067, https://doi.org/10.1016/j.ccst.2022.100067.

[23] A. Abdulrasheed, A.A. Jalil, Y. Gambo, M. Ibrahim, H.U. Hambali, M.Y. Shahul Hamid, A review on catalyst development for dry reforming of methane to syngas: Recent advances, Renewable and Sustainable Energy Reviews 108 (2019) 175-193. https://doi.org/10.1016/j.rser.2019.03.054.

[24] Z. Xie, Q. Liao, M. Liu, Z. Yang, L. Zhang, Micro-kinetic modeling study of dry reforming of methane over the Ni-based catalyst, Energ. Conver. Manage. 153 (2017) 526–537, https://doi.org/10.1016/j.enconman.2017.10.022.

[25] H. Huang, Y. Yu, M. Zhang, Mechanistic insight into methane dry reforming over cobalt: a density functional theory study, PCCP 22 (46) (2020) 27320–27331, https://doi.org/10.1039/c9cp07003f.

[26] W.-J. Jang, J.-O. Shim, H.-M. Kim, S.-Y. Yoo, H.-S. Roh, A review on dry reforming of methane in aspect of catalytic properties, Catal. Today 324 (2019) 15–26, https://doi.org/10.1016/j.cattod.2018.07.032.

[27] F. Sharifianjazi, A. Esmaeilkhanian, L. Bazli, S. Eskandarinezhad, S. Khaksar, P. Shafiee, M. Yusuf, B. Abdullah, P. Salahshour, F. Sadeghi, A review on recent advances in dry reforming of methane over Ni- and Co-based nanocatalysts, Int. J. Hydrogen Energy 47 (100) (2022) 42213–42233, https://doi.org/10.1016/j.ijhydene.2021.11.172.

[28] E. Yang, E. Nam, Y. Jo, K. An, Coke resistant NiCo/$CeO_2$ catalysts for dry reforming of methane derived from core@shell Ni@Co nanoparticles, Appl Catal B 339 (2023) 123152, https://doi.org/10.1016/j.apcatb.2023.123152.

[29] Z. Boukha, A. Bermejo-López, U. De-La-Torre, J.R. González-Velasco, Behavior of nickel supported on calcium-enriched hydroxyapatite samples for CCU-methanation and ICCU-methanation processes, Appl Catal B 338 (2023) 122989, https://doi.org/10.1016/j.apcatb.2023.122989.

[30] B. Shao, Z.Q. Wang, X.Q. Gong, H. Liu, F. Qian, P. Hu, J. Hu, Synergistic promotions between $CO_2$ capture and in-situ conversion on Ni-CaO composite catalyst, Nat. Commun. 14 (1) (2023) 996, https://doi.org/10.1038/s41467-023-36646-2.

[31] X. Zhao, S. Sun, Y. Zhang, Y. Wang, Y. Zhu, P. Williams, S. Guan, C. Wu, Synergistic performance of Ni-Ca based dual functional materials under the coexistence of moisture and oxygen in $CO_2$ source for integrated carbon capture and utilisation, Sep. Purif. Technol. 326 (2023) 124866, https://doi.org/10.1016/j.seppur.2023.124866.

[32] I. Wang, D. Li, S. Wang, Y. Wang, G. Lin, B. Yan, Z. Li, Limestone hydrogenation combined with reverse water–gas shift reaction under fluidized and iso-thermal conditions using MFB-TGA-MS, Chem. Eng. J. 472 (2023) 144822, https://doi.org/10.1016/j.cej.2023.144822.

[33] F. Wang, Y. Li, C. Zhang, J. Zhao, S. Niu, J. Qi, The mechanism for in-situ conversion of captured $CO_2$ by CaO to CO in presence of $H_2$ during calcium looping process based on DFT study, Fuel 329 (2022) 125402, https://doi.org/10.1016/j.fuel.2022.125402.

[34] S. Sun, Y. Zhang, C. Li, Y. Wang, C. Zhang, X. Zhao, H. Sun, C. Wu, Upgrading $CO_2$ from simulated power plant flue gas via integrated $CO_2$ capture and dry reforming of methane using Ni-CaO, Sep. Purif. Technol. 308 (2023) 122956, https://doi.org/10.1016/j.seppur.2022.122956.

[35] G. Kresse, J. Furthmüller, Efficiency of ab-initio total energy calculations for metals and semiconductors using a plane-wave basis set, Comput. Mater. Sci 6 (1) (1996) 15–50, https://doi.org/10.1016/0927-0256(96)00008-0.

[36] G. Kresse, D. Joubert, From ultrasoft pseudopotentials to the projector augmented-wave method, Phys. Rev. B 59 (3) (1999) 1758–1775, https://doi.org/10.1103/PhysRevB.59.1758.

[37] J.P. Perdew, K. Burke, M. Ernzerhof, Generalized gradient approximation made simple, Phys. Rev. Lett. 77 (18) (1996) 3865–3868, https://doi.org/10.1103/PhysRevLett.77.3865.

[38] S. Grimme, J. Antony, S. Ehrlich, H. Krieg, A consistent and accurate ab initio parametrization of density functional dispersion correction (DFT-D) for the 94 elements H-Pu, J. Chem. Phys. 132 (15) (2010) 154104, https://doi.org/10.1063/1.3382344.

[39] D.J. Chadi, Special points for brillouin-zone integrations, Phys. Rev. B 16 (4) (1977) 1746–1747, https://doi.org/10.1103/PhysRevB.16.1746.

[40] A.R.A. Astuti, I.G. Wenten, D. Ariono, D. Sasongko, W.H. Saputera, K. Khoiruddin, Advances in Carbon Control Technologies for Flue Gas Cleaning, Separation & Purification Reviews 1-30. https://doi.org/10.1080/15422119.2024.2328080.

[41] I. Wang, S. Huang, S. Wang, X. Bie, H. Zhou, Z. Li, Mechanistic study of integrated $CO_2$ capture and utilization over Cu and Al-modified calcined limestone with high stability using MFB-TGA-MS, Sep. Purif. Technol. 333 (2024) 125975, https://doi.org/10.1016/j.seppur.2023.125975.

[42] G. Liu, Z. Hu, G. Lisak, $CO_2$ capture and utilization through isothermal carbonation-calcination looping integrated with MSW pyrolysis volatile reforming, Chem. Eng. J. 482 (2024) 149164, https://doi.org/10.1016/j.cej.2024.149164.

[43] T. Bauer, D. Laing, R.J.M.S.C. Tamme, Technology, Recent progress in alkali nitrate/nitrite developments for solar thermal power applications, (2014) 543-553.

[44] M. Krodel, A. Landuyt, P.M. Abdala, C.R. Muller, Mechanistic understanding of CaO-based sorbents for high-temperature $CO_2$ capture: advanced characterization and prospects, ChemSusChem 13 (23) (2020) 6259–6272, https://doi.org/10.1002/cssc.202002078.

[45] Q. Zhang, M. Akri, Y. Yang, B. Qiao, Atomically dispersed metals as potential coke-resistant catalysts for dry reforming of methane, Cell Reports Phys. Sci. 4 (3) (2023) 101310, https://doi.org/10.1016/j.xcrp.2023.101310.

[46] M. Msheik, S. Rodat, S. Abanades, Experimental comparison of solar methane pyrolysis in gas-phase and molten-tin bubbling tubular reactors, Energy 260 (2022), https://doi.org/10.1016/j.energy.2022.124943.

[47] M. Krödel, L. Abduly, M. Nadjafi, A. Kierzkowska, A. Yakimov, A.H. Bork, F. Donat, C. Copéret, P.M. Abdala, C.R. Müller, Structure of Na species in promoted CaO-based sorbents and their effect on the rate and extent of the CO2 uptake, Adv. Funct. Mater. 33 (40) (2023) 2302916, https://doi.org/10.1002/adfm.202302916.

[48] Q. Tang, Z. Shen, L. Huang, T. He, H. Adidharma, A.G. Russell, M. Fan, Synthesis of methanol from $CO_2$ hydrogenation promoted by dissociative adsorption of hydrogen on a $Ga_3Ni_5$ surface, PCCP 19 (28) (2017) 18539–18555, https://doi.org/10.1039/c7cp03231e.

[49] B. Jin, T. Ouyang, Z. Zhang, Y. Zhao, H. Zhang, W. Yao, G. Huang, Z. Liang, Prussian blue derived Ca-Fe bifunctional materials for chemical looping $CO_2$ capture and in-situ conversion, Sep. Purif. Technol. (2023) 123975, https://doi.org/10.1016/j.seppur.2023.123975.

[50] Y. Guo, G. Wang, J. Yu, P. Huang, J. Sun, R. Wang, T. Wang, C. Zhao, Tailoring the performance of Ni-CaO dual function materials for integrated $CO_2$ capture and conversion by doping transition metal oxides, Sep. Purif. Technol. 305 (2023) 122455, https://doi.org/10.1016/j.seppur.2022.122455.

[51] H. Sun, Y. Wang, S. Xu, A.I. Osman, G. Stenning, J. Han, S. Sun, D. Rooney, P. T. Williams, F. Wang, C. Wu, Understanding the interaction between active sites and sorbents during the integrated carbon capture and utilization process, Fuel 286 (2021) 119308, https://doi.org/10.1016/j.fuel.2020.119308.

[52] D. Pinto, L. Hu, A. Urakawa, Enabling complete conversion of CH4 and CO2 in dynamic coke-mediated dry reforming (DC-DRM) on Ni catalysts, Chem. Eng. J. 474 (2023), https://doi.org/10.1016/j.cej.2023.145641.

[53] S. Sun, Y. Wang, Y. Xu, H. Sun, X. Zhao, Y. Zhang, X. Yang, X. Bie, M. Wu, C. Zhang, Y. Zhu, Y. Xu, H. Zhou, C. Wu, Ni-functionalized Ca@Si yolk-shell nanoreactors for enhanced integrated CO2 capture and dry reforming of methane via confined catalysis, Appl. Catal. b: Environ. Energy 348 (2024) 123838, https://doi.org/10.1016/j.apcatb.2024.123838.

[54] S. Sun, C. Zhang, Y. Wang, X. Zhao, H. Sun, C. Wu, $CO_2$ capture from $H_2O$ and $O_2$ containing flue gas integrating with dry reforming methane using Ni-doping CaO dual functional materials, Chem. Eng. J. 468 (2023) 143712, https://doi.org/10.1016/j.cej.2023.143712.

[55] Y. Yuan, Y. Li, L. Duan, H. Liu, J. Zhao, Z. Wang, CaO/Ca(OH)2 thermochemical heat storage of carbide slag from calcium looping cycles for CO2 capture, Energ. Conver. Manage. 174 (2018) 8–19, https://doi.org/10.1016/j.enconman.2018.08.021.

[56] O.A. Maslova, M.R. Ammar, G. Guimbretière, J.N. Rouzaud, P. Simon, Determination of crystallite size in polished graphitized carbon by Raman spectroscopy, Phys. Rev. B 86 (13) (2012) 134205, https://doi.org/10.1103/PhysRevB.86.134205.

[57] J.S. Park, A. Reina, R. Saito, J. Kong, G. Dresselhaus, M.S. Dresselhaus, G′ band Raman spectra of single, double and triple layer graphene, Carbon 47 (5) (2009) 1303–1310, https://doi.org/10.1016/j.carbon.2009.01.009.

[58] A. Jorio, A.G. Souza Filho, G. Dresselhaus, M.S. Dresselhaus, A.K. Swan, M.S. Ünlü, B.B. Goldberg, M.A. Pimenta, J.H. Hafner, C.M. Lieber, R. Saito, G-band resonant Raman study of 62 isolated single-wall carbon nanotubes, Phys. Rev. B 65 (15) (2002) 155412, https://doi.org/10.1103/PhysRevB.65.155412.

[59] F.A. Al-Doghachi, A. Islam, Z. Zainal, M.I. Saiman, Z. Embong, Y.H. Taufiq-Yap, High coke-resistance Pt/Mg1-xNixO catalyst for dry reforming of methane, PLoS One 11 (1) (2016) e0145862, https://doi.org/10.1371/journal.pone.0145862.

[60] H. Wang, S. Kim, E. Sasmaz, Numerical investigation of the reaction kinetics of dry reforming of methane over the yolk–shell and single-atom alloy catalysts, Chem. Eng. J. 450 (2022) 138111, https://doi.org/10.1016/j.cej.2022.138111.

[61] R.E. Owen, Y.S. Zhang, T.P. Neville, G. Manos, P.R. Shearing, D.J.L. Brett, J. J. Bailey, Visualising coke-induced degradation of catalysts used for $CO_2$-reforming of methane with X-ray nano-computed tomography, Carbon Capture Science & Technology 5 (2022) 100068, https://doi.org/10.1016/j.ccst.2022.100068.

[62] B. Mile, D. Stirling, M.A. Zammitt, A. Lovell, M. Webb, The location of nickel oxide and nickel in silica-supported catalysts: Two forms of "NiO" and the assignment of temperature-programmed reduction profiles, J. Catal. 114 (2) (1988) 217–229, https://doi.org/10.1016/0021-9517(88)90026-7.

[63] B. Zhang, R. Shi, W. Duan, Z. Luo, Z.-y. Lu, S.J.R.a. Cui, Direct comparison between chemisorption and physisorption: a study of poly (ethylene glycol) by means of single-molecule force spectroscopy, 7(54) (2017) 33883-33889.

[64] C. Wilhelm, J.-L. Gardette, Infrared analysis of the photochemical behaviour of segmented polyurethanes: 1. aliphatic poly(ester-urethane), Polymer 38(16) (1997) 4019–4031, https://doi.org/10.1016/S0032-3861(96)00984-6.

[65] O.I. Malyi, P. Thiyam, M. Bostrom, C. Persson, A first principles study of CO2 adsorption on alpha-SiO2(001) surfaces, PCCP 17 (31) (2015) 20125–20133, https://doi.org/10.1039/c5cp02279g.

[66] R. Ye, L. Ma, X. Hong, T.R. Reina, W. Luo, L. Kang, G. Feng, R. Zhang, M. Fan, R. Zhang, J. Liu, Boosting low-temperature $CO_2$ hydrogenation over Ni-based catalysts by tuning strong metal-support interactions, Angew. Chem. Int. Ed. Engl. 63 (3) (2024) e202317669, https://doi.org/10.1002/anie.202317669.

[67] R.-P. Ye, W. Gong, Z. Sun, Q. Sheng, X. Shi, T. Wang, Y. Yao, J.J. Razink, L. Lin, Z. Zhou, H. Adidharma, J. Tang, M. Fan, Y.-G. Yao, Enhanced stability of Ni/$SiO_2$ catalyst for $CO_2$ methanation: derived from nickel phyllosilicate with strong metal-support interactions, Energy 188 (2019), https://doi.org/10.1016/j.energy.2019.116059.

[68] F. Geobaldo, B. Onida, P. Rivolo, F. Di Renzo, F. Fajula, E. Garrone, Nature and reactivity of Co species in a cobalt-containing beta zeolite: an FTIR study, Catal. Today 70 (1) (2001) 107–119, https://doi.org/10.1016/S0920-5861(01)00411-4.

[69] H. Sun, C. Wang, S. Sun, A.T. Lopez, Y. Wang, J. Zeng, Z. Liu, Z. Yan, C.M. A. Parlett, C. Wu, XAS/DRIFTS/MS spectroscopy for time-resolved operando study of integrated carbon capture and utilisation process, Sep. Purif. Technol. 298 (2022) 121622, https://doi.org/10.1016/j.seppur.2022.121622.

[70] H.-Q. Yang, C.-W. Hu, S. Qin, Theoretical study on the reaction mechanism of $CH_4$ with CaO, Chem. Phys. 330 (3) (2006) 343–348, https://doi.org/10.1016/j.chemphys.2006.07.046.

[71] K.I. Hadjiivanov, M.M. Kantcheva, D.G. Klissurski, Faraday Transactions, IR study of CO adsorption on Cu-ZSM-5 and CuO/SiO2 catalysts: σ and π components of the Cu+—CO bond, J. Chem. Soc. Faraday Trans. 92 (22) (1996) 4595–4600.

[72] A. Föhlisch, M. Nyberg, J. Hasselström, O. Karis, L.G.M. Pettersson, A. Nilsson, How carbon monoxide adsorbs in different sites, Phys. Rev. Lett. 85 (15) (2000) 3309–3312, https://doi.org/10.1103/PhysRevLett.85.3309.

[73] Y.-T. Su, Y.-H. Huang, H.A. Witek, Y.-P. Lee, Infrared Absorption Spectrum of the Simplest Criegee Intermediate $CH_2OO$, 340(6129) (2013) 174-176. https://doi.org/doi:10.1126/science.1234369.

[74] A. Michaelides, P. Hu, Softened C-H modes of adsorbed methyl and their implications for dehydrogenation: an ab initio study, J. Chem. Phys. 114 (6) (2001) 2523–2526, https://doi.org/10.1063/1.1345907.

[75] J.T. Kloprogge, R.L. Frost, Infrared emission spectroscopic study of the dehydroxylation of synthetic, Mg/al and Mg/zn/al-Hydrotalcites 1 (7) (1999) 1641–1647.

[76] A. Koteja, J. Matusik, Preparation of azobenzene-intercalated kaolinite and monitoring of the photoinduced activity, Clay Miner. 54 (1) (2019) 57–66, https://doi.org/10.1180/clm.2019.6.